A NURBS-based finite element model applied to geometrically nonlinear elastodynamics using a corotational approach

L. F. R. Espath[1,*,†], A. L. Braun[1], A. M. Awruch[1] and L. D. Dalcin[2,3]

[1]*Graduate Program in Civil Engineering (PPGEC), Federal University of Rio Grande do Sul (UFRGS), Porto Alegre, RS, Brazil*
[2]*National Scientific and Technical Research Council (CONICET), Santa Fe, Argentina*
[3]*Center for Numerical Porous Media, King Abdullah University of Science and Technology, Thuwal, Saudi Arabia*

SUMMARY

A numerical model to deal with nonlinear elastodynamics involving large rotations within the framework of the finite element based on NURBS (Non-Uniform Rational B-Spline) basis is presented. A comprehensive kinematical description using a corotational approach and an orthogonal tensor given by the exact polar decomposition is adopted. The state equation is written in terms of corotational variables according to the hypoelastic theory, relating the Jaumann derivative of the Cauchy stress to the Eulerian strain rate.

The generalized-α method (Gα) method and Generalized Energy-Momentum Method with an additional parameter (GEMM+ξ) are employed in order to obtain a stable and controllable dissipative time-stepping scheme with algorithmic conservative properties for nonlinear dynamic analyses.

The main contribution is to show that the energy–momentum conservation properties and numerical stability may be improved once a NURBS-based FEM in the spatial discretization is used. Also it is shown that high continuity can postpone the numerical instability when GEMM+ξ with consistent mass is employed; likewise, increasing the continuity class yields a decrease in the numerical dissipation. A parametric study is carried out in order to show the stability and energy budget in terms of several properties such as continuity class, spectral radius and lumped as well as consistent mass matrices. Copyright © 2015 John Wiley & Sons, Ltd.

1. INTRODUCTION

The development of numerical algorithms to simulate the dynamic response of linear and nonlinear elastic bodies is a major topic in the field of elastodynamics. Traditional time-stepping schemes, despite having excellent stability properties in the linear range, are usually subject to numerical instabilities when they are applied to nonlinear problems using numerical models based on the finite element method (FEM). Investigations on elastodynamics using isogeometric analysis may be performed in order to study influences of the isogeometric formulation over numerical issues such as stability and accuracy, where aspec ts related to the time integration process are also extremely important.

---

*Correspondence to: L. F. R. Espath, Graduate Program in Civil Engineering (PPGEC), Federal University of Rio Grande do Sul (UFRGS), Av. Osvaldo Aranha, 99, 3o andar, 90035-190 Porto Alegre, RS, Brazil.
†E-mail: espath@gmail.com

The need for numerical dissipation was soon recognized when unconditional time-stepping schemes were applied to finite element models in order to solve dynamic problems with implicit algorithms. It was observed that large modeling errors associated with the high-frequency range are introduced by the spatial discretization procedure owing to deficiencies found in the element formulation to reproduce the higher modes accurately. In this sense, although the standard Newmark's method presented no numerical dissipation, a formulation with controllable numerical damping was proposed by Newmark [1]. Later, the Newmark's method and other early algorithms with numerical damping such as the Wilson's method and the Houbolt's method were investigated by Goudreau and Taylor [2], where the introduction of a controlled degree of damping to reduce the spurious action of the higher modes was recommended. However, unconditionally stable algorithms lead to period elongation, and the second-order accuracy is lost because of the introduction of numerical dissipation. This drawback was resolved with the method proposed by Hilber *et al.* [3], which combines unconditional stability, second-order accuracy, and numerical dissipation of higher modes. A similar improvement was obtained with the formulation introduced by Wood *et al.* [4], and a generalization of the methods presented in [3] and [4], called the generalized-α method (Gα), was provided by Chung and Hulbert [5]. The Gα method leads to second-order accuracy, and optimized behavior for the numerical dissipation is obtained when linear problems are analyzed, where minimal dissipation is observed for lower modes while maximal dissipation is verified for higher modes.

The development of energy-conserving algorithms was motivated by the work presented by Belytschko and Schoeberle [6], who concluded that a numerical algorithm is stable in terms of energy if the sum of kinetic and internal energies within each time step is bounded by the external work and the kinetic and internal energies evaluated in the previous time step. Moreover, it was verified that algorithms presenting unconditional stability for applications in linear dynamics are frequently subject to numerical instability when the nonlinear case is analyzed. Following the energy criterion introduced in [6], an energy-conserving scheme for nonlinear dynamics where the trapezoidal rule is extended by using the Lagrange multiplier method to enforce energy conservation was proposed by Hughes *et al.* [7]. Nevertheless, Ortiz [8] demonstrated that energy conservation is not a sufficient condition for maintaining numerical stability in the nonlinear range. The constraint energy method presented in [7] conserves the total energy perfectly but leads to failure in the iteration procedure related to the Newton–Raphson linearization, as was observed by Kuhl and Ramm [9].

Indeed, Simo and Tarnow [10] had already noticed the importance of momentum conservation by proposing the energy–momentum method, which conserves total energy as well as linear and angular momentum. Furthermore, second-order accuracy is also preserved. The energy–momentum method was developed considering the midpoint rule to evaluate the internal forces in every time step of the time integration process in order to reach energy conservation algorithmically, because it was concluded that the stress update procedure is crucial to obtain a numerical algorithm with energy–momentum conservation. The original formulation was introduced using a constitutive model for Saint Venant–Kirchhoff materials, which was extended to arbitrary hyperelastic materials by Gonzales [11], who proposed a modified evaluation of the stress tensor employing discrete derivative to describe the required form for the algorithmic update of the second Piola–Kirchhoff stress tensor. Later, Laursen and Meng [12] reformulated the stress update scheme presented in [10] to account for general hyperelastic models properly, where some restrictions found in the original formulation were removed. An energy–momentum-conserving algorithm for hypoelastic constitutive models was developed by Noels *et al.* [13] by using a new expression for evaluating the internal forces at element level. A hypoelastic formulation for applications in nonlinear elastodynamics using the eight-node hexahedral element with one-point quadrature techniques was used by Braun and Awruch [14]. According to Romero [15], there are infinite ways to obtain second-order accuracy as well as energy and momentum conservation algorithms, whereas the characterization of the conserving stress as a minimization problem leads to that conclusion.

Although the conservation of energy and momentum is mandatory in order to obtain a stable numerical algorithm, some amount of numerical dissipation must be introduced in the model to damp out spurious contributions of the high-frequency range to the dynamic response, which are induced because of problems related to the finite element discretization of the spatial domain. On

the other hand, it is well known that classical dissipative methods may fail when they are applied to nonlinear problems and loss of accuracy is generally observed in these cases. This situation motivated the development of energy-dissipative momentum-conserving algorithms, where momentum is conserved, energy dissipation is controlled, and order of accuracy is maintained. The constraint energy–momentum method was proposed in [9], which is a time-stepping scheme combining conservation and dissipation properties, where energy and momentum are enforced considering the constraint energy methodology proposed in [7] and the Gα method given in [5] is used in order to obtain a dissipative time integration model. Optimized parameters for the α methods were determined, leading to an integration process with less numerical dissipation for lower frequencies and more dissipation on higher frequencies of the energy spectrum. An algorithm based on controllable numerical dissipation and on the energy–momentum method introduced in [10] was presented by Kuhl and Crisfield [16] considering a nonlinear version of the Gα method. The numerical scheme was called the generalized energy–momentum method (GEMM), and applications for shell dynamics were later investigated by Kuhl and Ramm [17] with an additional dissipative parameter, yielding the generalized energy–momentum method + ξ (GEMM+ξ). The energy–momentum method, proposed in [10], to include numerical dissipation by using a damping parameter that only affects the second Piola–Kirchhoff stress tensor was modified by Armero and Pectocz [18] and also by Crisfield *et al.* [19]. Nevertheless, the so-called modified energy–momentum method is only first-order accurate. In order to circumvent this drawback, a dissipative time-stepping algorithm with energy conservation properties that also preserves second-order accuracy was developed by Armero and Romero [20]. Reviews on energy–momentum and dissipative methods may be found in [16, 21], and [22].

In the present work, a non-uniform rational B-spline (NURBS)-based finite element model is developed for applications in nonlinear elastodynamics. The kinematic description of the continuum is performed using the corotational approach. A hypoelastic constitutive model is adopted using corotational stress and strain tensors, where the small strain hypothesis and large displacements and rotations are considered. This comprehensive corotational kinematic description is performed using an orthogonal tensor given by the exact polar decomposition for transformations of the coordinate system. The state equation is written in terms of corotational variables according to the linear elastic theory, relating the Jaumann derivative of the Cauchy stress to the Eulerian strain rate. The numerical model is obtained by applying the Bubnov–Galerkin weighted residual method over the Cauchy's equation of motion, and a Newton–Raphson scheme is adopted to linearize the residual vector in the nonlinear range. Geometry and solution fields are approximated using NURBS basis functions according to the isoparametric concept. The Gα method and GEMM+ξ are implemented into the IsoGeometric formulation in order to obtain stable and controllable dissipative schemes for time integration. Additional information about NURBS solids and this NURBS finite element model for nonlinear static analysis may be found in [23].

The influence of aspects related to the IsoGeometric discretization is investigated for numerical applications where numerical instabilities are expected. An important improvement can be noted in both temporal integrators Gα and GEMM+ξ when a NURBS description is adopted. We use as a baseline of comparison the classical works of Kuhl and Ramm [9, 17] where it is shown in particular that Gα in nonlinear regime cannot fulfill both the numerical stability and the energy–momentum conservation. In the present work, it is shown in particular that a high continuity can postpone the numerical instability when GEMM+ξ with consistent mass is employed; likewise, increasing the continuity class yields a decrease in the numerical dissipation. Although a high degree of spatial discretization may be considered expensive, it is important to notice that shell and beam structures may be subject to locking phenomena if high-order discretization is not employed once they are modeled as thin solids. A parametric study is carried out in order to show the stability and energy budget in terms of several properties such as continuity class of basis, function spectral radius and lumped as well as consistent mass matrices.

2. THEORETICAL ASPECTS

2.1. Governing equations for elastodynamics and corotational approach

Problems on elastodynamics may be formulated considering the Cauchy's equation of motion, where mass and energy conservation must be also enforced over the volume of the body (for instance, [24]). Considering a classical Lagrangian kinematical description in the Cartesian coordinate system and in the absence of temperature changes, the system of governing equations is given by the following expressions:

$$\int_{\Omega_0} \rho\left(\underline{\mathbf{X}}, t_0\right) \mathrm{d}\Omega = \int_{\Omega} \rho\left(\underline{\mathbf{x}}, t\right) \mathrm{d}\Omega \quad \forall t \in [t_0, t] \tag{1a}$$

$$\rho\ddot{\underline{\mathbf{u}}} - \mathbf{div}\ \underline{\underline{\sigma}} - \underline{\mathbf{b}} = \underline{\mathbf{0}} \quad \text{in} \quad \Omega \times [t_0, t] \tag{1b}$$

$$\underline{\mathbf{u}} = \bar{\underline{\mathbf{u}}} \quad \text{on} \quad \Gamma_D \times [t_0, t] \tag{1c}$$

$$\underline{\underline{\sigma}} \cdot \underline{\mathbf{n}} = \bar{\underline{\mathbf{t}}} \quad \text{on} \quad \Gamma_N \times [t_0, t] \tag{1d}$$

$$\underline{\mathbf{u}}\left(\underline{\mathbf{x}}, t_0\right) = \bar{\underline{\mathbf{u}}}_0 \quad \text{in} \quad \Omega \tag{1e}$$

$$\dot{\underline{\mathbf{u}}}\left(\underline{\mathbf{x}}, t_0\right) = \bar{\dot{\underline{\mathbf{u}}}}_0 \quad \text{in} \quad \Omega \tag{1f}$$

where Equations (1a) and (1b) represent mass and momentum balances over the spatial domain $\Omega(t)$ corresponding to the body, respectively, with the first-order tensors $\underline{\mathbf{X}}$ and $\underline{\mathbf{x}}$ containing components of the material (X_i) and spatial (x_i) coordinates in the Cartesian coordinate system, t denotes time, ρ is the specific mass of the body, $\underline{\mathbf{b}}$ is the first-order tensor of body forces per unit mass, the second-order tensor $\underline{\underline{\sigma}}$ contains components of the Cauchy stress tensor, and the first-order tensors $\underline{\mathbf{u}}$ and $\ddot{\underline{\mathbf{u}}}$ are the displacement and the second time derivative of the displacement. The boundary conditions are given according to Equations (1c) and (1d), where the first-order tensors $\bar{\underline{\mathbf{u}}}$ and $\bar{\underline{\mathbf{t}}}$ are the prescribed Dirichlet and Neumann boundary conditions, over the boundaries Γ_D and Γ_N, respectively, taking into account that $\underline{\mathbf{n}}$ is the unit outward normal defined on boundary Γ_N. Equations (1e) and (1f) specify the initial conditions ($t = t_0$; $\Omega = \Omega_0$) for the displacement and its first time-derivative fields. In addition, $\Gamma_D \bigcup \Gamma_N = \Gamma$ and $\Gamma_D \bigcap \Gamma_N = \emptyset$. It is important to notice that the equilibrium equation, which is derived from the Cauchy's equation of motion, is defined taking into account the current configuration of the body (Ω).

In the present model, geometrically nonlinear problems are analyzed taking into account the corotational approach (any tensor field in corotational frame is identified by $(\hat{\cdot})$), where stress and strain are described according to a coordinate system locally attached to every quadrature point. Consequently, a linear constitutive model restricted to small strains can be adopted in order to relate strain and stress measures, which may be written as

$$\hat{\underline{\underline{\sigma}}} = \hat{\underline{\underline{\mathbf{C}}}}^{mat} : \hat{\underline{\underline{\epsilon}}} = \lambda \mathrm{tr}(\hat{\underline{\underline{\epsilon}}})\underline{\underline{\mathbf{1}}} + 2\mu\hat{\underline{\underline{\epsilon}}} \tag{2}$$

where $\hat{\underline{\underline{\sigma}}}$ and $\hat{\underline{\underline{\epsilon}}}$ are the Cauchy stress tensor and the small strain tensor, both defined in the corotational system. $\hat{\underline{\underline{\mathbf{C}}}}^{mat}$ is the fourth-order elastic tensor, which may be described in terms of the Lamé constants, λ and μ.

Theoretically, the motion of a continuum can be decomposed into rigid body motion and pure deformation. This separation of rigid body and purely deformational motions is originated by assumption of large rotations. Once the spatial discretization of the problem is fine enough, this decomposition can be performed at the quadrature level and consequently, in a corotational coordinate system, where the pure deformation part is always a small quantity with respect to the element dimensions. The corotational description maintains orthogonality of the reference frame, which leads to exact decomposition of the motion into rigid body and deformational parts. In this sense, an elastic constitutive formulation is very effective for corotational descriptions, because the nonlinear problem can be posed in rate form by considering the small strain hypothesis and an objective rate of the Cauchy stress tensor.

Assuming that all kinematical variables at the previous configuration t_n of the body are known, the displacement field at the end of the current load step can be obtained from integration of the strain rate tensor over the time interval defining the present load increment $[t_n, t_{n+1}]$. In addition, this integration to obtain the strain increment must be performed in the corotational coordinate system, where only the deformational part of the incremental displacement field is considered. The strain rate tensor in the corotational system is defined as

$$\hat{\underline{\underline{d}}} = \frac{1}{2}\left[\frac{\partial \hat{\underline{v}}^{def}}{\partial \hat{\underline{x}}} + \left(\frac{\partial \hat{\underline{v}}^{def}}{\partial \hat{\underline{x}}}\right)^t\right] \tag{3}$$

where $\hat{\underline{v}}^{def}$ represents the velocity field associated with the deformation part of the motion in the corotational system. In order to obtain strain increments, some methodology must be adopted to integrate the strain tensor over the time interval $[t_n, t_{n+1}]$. In the present work, the midpoint integration proposed by Hughes and Winget [25] is used, where the velocity is assumed to be constant within the time interval and the reference configuration is attached to the intermediate configuration $t_{n+\frac{1}{2}}$ in the corotational system. According to the midpoint integration, the strain increment may be obtained from

$$\int_{t_n}^{t_{n+1}} \hat{\underline{\underline{d}}}\, d\tau = \frac{1}{2}\left[\frac{\partial \Delta \hat{\underline{u}}^{def}}{\partial \hat{\underline{x}}_{n+\frac{1}{2}}} + \left(\frac{\partial \Delta \hat{\underline{u}}^{def}}{\partial \hat{\underline{x}}_{n+\frac{1}{2}}}\right)^t\right] = \underline{\underline{\Delta \hat{\epsilon}}} \tag{4}$$

where $\Delta \hat{\underline{u}}^{def}$ is the deformation part of the displacement increment in the corotational system and $\hat{\underline{x}}_{n+\frac{1}{2}}$ is the intermediate configuration of the body defined in the corotational system, which can be determined according to the following expression:

$$\hat{\underline{x}}_{n+\frac{1}{2}} = \underline{\underline{R}}_{n+\frac{1}{2}} \cdot \underline{x}_{n+\frac{1}{2}} = \frac{1}{2}\underline{\underline{R}}_{n+\frac{1}{2}} \cdot \left(\underline{x}_n + \underline{x}_{n+1}\right) \tag{5}$$

where $\underline{\underline{R}}_{n+\frac{1}{2}}$ is the orthogonal transformation tensor performing rotation from the global system to the corotational system defined locally at the intermediate configuration $t_{n+\frac{1}{2}}$. The displacement increment referring to the present time interval $[t_n, t_{n+1}]$ can be decomposed as follows:

$$\underline{\Delta u} = \underline{\Delta u}^{def} + \underline{\Delta u}^{rot} \tag{6}$$

where $\underline{\Delta u}^{def}$ and $\underline{\Delta u}^{rot}$ are, respectively, the deformation and rotation parts of the displacement increment defined in the global coordinate system. It is important to notice that the decomposition described in Equation (6) is locally performed at element level. The deformation displacement increment in the corotational system can be obtained from the following expression:

$$\underline{\Delta \hat{u}}^{def} = \underline{\underline{R}}_{n+\frac{1}{2}} \cdot \underline{\Delta u}^{def} = \hat{\underline{x}}_{n+1} - \hat{\underline{x}}_n \tag{7}$$

where the transformation tensor $\underline{\underline{R}}$ is evaluated at the intermediate configuration $t_{n+\frac{1}{2}}$ of the current time interval $[t_n, t_{n+1}]$, because the strain rate tensor must be referred to the body configuration at $t_{n+\frac{1}{2}}$. Coordinates corresponding to the previous and current configurations of the body in the corotational system are obtained with following transformations:

$$\hat{\underline{x}}_n = \underline{\underline{R}}_n \cdot \underline{x}_n; \qquad \hat{\underline{x}}_{n+1} = \underline{\underline{R}}_{n+1} \cdot \underline{x}_{n+1} \tag{8}$$

where $\underline{\underline{R}}_n$ and $\underline{\underline{R}}_{n+1}$ are orthogonal transformation tensors performing rotations from the global system to the corotational system defined locally at t_n and t_{n+1}, respectively.

After determining the strain increment in the corotational system, strain and stress updates can be performed with the following equations:

$$\hat{\underline{\underline{\epsilon}}}_{n+1} = \hat{\underline{\underline{\epsilon}}}_n + \underline{\underline{\Delta \hat{\epsilon}}} \tag{9a}$$

$$\hat{\underline{\underline{\sigma}}}_{n+1} = \hat{\underline{\underline{\sigma}}}_n + \underline{\underline{\Delta \hat{\sigma}}} \tag{9b}$$

where n and $n + 1$ denote the previous and current configurations of the body in the corotational system, respectively. It is well known that the Cauchy stress tensor in the corotational system is frame-invariant, because stress measures are not affected by rigid body motions, but the rate of the Cauchy stress tensor is not. Therefore, in order to obtain an incrementally objective constitutive formulation, the Jaumann rate tensor is adopted in this work, which may be described as follows:

$$\overset{\circ}{\hat{\underline{\underline{\sigma}}}}{}^{J} = \dot{\hat{\underline{\underline{\sigma}}}} + \hat{\underline{\underline{\sigma}}} \cdot \hat{\underline{\underline{\Omega}}} - \hat{\underline{\underline{\Omega}}} \cdot \hat{\underline{\underline{\sigma}}} \tag{10}$$

where spin tensor $\hat{\underline{\underline{\Omega}}}$ is the antisymmetric part of the spatial velocity gradient tensor $\hat{\underline{\underline{L}}}$ defined in the corotational system. The corotational spin tensor must be also integrated over the time interval $[t_n, t_{n+1}]$ considering the same midpoint rule adopted in Equation (4).

The orthogonal transformation tensor $\underline{\underline{R}}$ may be evaluated using several methods. In the present work, a classical polar decomposition theorem is utilized, where spectral decomposition or eigen-projection of the right Cauchy–Green deformation tensor $\underline{\underline{C}}$ is adopted to obtain the right stretch tensor $\underline{\underline{U}}$.

Being the deformation gradient tensor defined as

$$\underline{\underline{F}} = \frac{\partial \underline{x}}{\partial \underline{X}} \tag{11}$$

it can be decomposed uniquely (while $\underline{\underline{F}}$ is injective) into a symmetric part and an orthogonal part

$$\underline{\underline{F}} = \underline{\underline{Q}} \cdot \underline{\underline{U}} = \underline{\underline{V}} \cdot \underline{\underline{Q}} \tag{12}$$

where $\underline{\underline{Q}}$ is an orthogonal tensor and $\underline{\underline{U}}$ and $\underline{\underline{V}}$ are the right and left stretch tensors. Recall that the right Cauchy–Green deformation tensor is defined as

$$\underline{\underline{C}} = \underline{\underline{F}}^{t} \cdot \underline{\underline{F}} \tag{13}$$

Then, taking into account Equation (12)

$$\underline{\underline{C}} = \underline{\underline{U}}^{t} \cdot \underline{\underline{Q}}^{t} \cdot \underline{\underline{Q}} \cdot \underline{\underline{U}} = \underline{\underline{U}}^{2} \tag{14}$$

and from spectral decomposition or eigenprojection of $\underline{\underline{C}}$, the following expression may be written:

$$\underline{\underline{C}} = \lambda_i^2 \, \underline{N}_i \otimes \underline{N}_i = \underline{\underline{U}}^{2} \tag{15}$$

where λ_i^2 and $\underline{N}_i$ are eigenvalues and eigenvectors of $\underline{\underline{C}}$, respectively. Then, the orthogonal tensor is evaluated as

$$\underline{\underline{Q}} = \underline{\underline{F}} \cdot \underline{\underline{U}}^{-1} = \underline{\underline{F}} \cdot \left(\lambda_i^{-1} \, \underline{N}_i \otimes \underline{N}_i \right) \tag{16}$$

The transformation tensor utilized in the corotational formulation is obtained considering that $\underline{\underline{R}} = \underline{\underline{Q}}^{t}$.

2.2. The numerical model

A numerical model based on IsoGeometric analysis may be constructed using variational principles in the same form as that used by the FEM, which is equivalent to considering the corresponding weak forms obtained from the Galerkin method applied to the governing equations. In elastodynamics, the Hamilton's principle can be adopted according to the following expression:

$$\int_{t_0}^{t} \delta(K - \pi) \, dt + \int_{t_0}^{t} \delta W_d \, dt \tag{17}$$

with

$$K = \frac{1}{2}\int_\Omega \rho\underline{\dot{\mathbf{u}}}\cdot\underline{\dot{\mathbf{u}}}\,\mathrm{d}\Omega \quad \delta K = \int_\Omega \rho\underline{\delta\dot{\mathbf{u}}}\cdot\underline{\dot{\mathbf{u}}}\,\mathrm{d}\Omega \tag{18a}$$

$$\pi = \int_\Omega U(\underline{\underline{\epsilon}})\,\mathrm{d}\Omega - \int_\Omega \underline{\mathbf{u}}\cdot\underline{\mathbf{b}}\,\mathrm{d}\Omega - \int_\Gamma \underline{\mathbf{u}}\cdot\underline{\mathbf{t}}\,\mathrm{d}\Gamma \quad \delta\pi = \int_\Omega \underline{\underline{\delta\epsilon}}:\underline{\underline{\sigma}}\,\mathrm{d}\Omega - \int_\Omega \underline{\delta\mathbf{u}}\cdot\underline{\mathbf{b}}\,\mathrm{d}\Omega - \int_{\Gamma_N} \underline{\delta\mathbf{u}}\cdot\underline{\mathbf{t}}\,\mathrm{d}\Gamma \tag{18b}$$

$$W_d = -\int_\Omega \underline{\mathbf{u}}\cdot\underline{\mathbf{f}}_d\,\mathrm{d}\Omega \quad \delta W_d = -\int_\Omega \underline{\delta\mathbf{u}}\cdot\underline{\mathbf{f}}_d\,\mathrm{d}\Omega \tag{18c}$$

where K and π are the kinetic energy and the total potential energy, respectively, with δK and $\delta\pi$ denoting its corresponding variations, W_d is the work done by any non-conserving force of the system and δW_d is the respective variation, $U(\underline{\underline{\epsilon}}) = \int_\Omega \underline{\underline{\sigma}}:\underline{\underline{\epsilon}}\,\mathrm{d}\Omega$ is the strain energy density function, and $\underline{\mathbf{f}}_d$ is the vector of non-conserving forces, including viscous damping $\underline{\mathbf{f}}_d = \chi\underline{\dot{\mathbf{u}}}$. The displacement variations $\underline{\delta\mathbf{u}}$ must vanish at the time limits t_0 and t_f and also on boundary Γ_D, where Dirichlet boundary conditions are imposed.

The semidiscrete system of momentum equations is obtained taking into account that they are discrete in space but continuous in time. The space discretization is performed here considering the Bubnov–Galerkin method applied into the context of IsoGeometric analysis, where the displacement variations associated with the variational form (Equation (17)) assume the role of weight functions. By integrating by parts the kinetic energy variation presented in Equation (17) and considering the restrictions imposed on the displacement variations $\underline{\delta\mathbf{u}}$ at the time limits t_0 and t_f, the following expression is obtained:

$$\int_{t_0}^t \left(\int_\Omega \rho\underline{\delta\mathbf{u}}\cdot\underline{\ddot{\mathbf{u}}}\,\mathrm{d}\Omega + \int_\Omega \underline{\delta\mathbf{u}}\cdot\chi\underline{\dot{\mathbf{u}}}\,\mathrm{d}\Omega - \int_\Omega \underline{\underline{\delta\epsilon}}:\underline{\underline{\sigma}}\,\mathrm{d}\Omega + \int_\Omega \underline{\delta\mathbf{u}}\cdot\underline{\mathbf{b}}\,\mathrm{d}\Omega + \int_{\Gamma_N} \underline{\delta\mathbf{u}}\cdot\underline{\mathbf{t}}\,\mathrm{d}\Gamma \right)\mathrm{d}t = 0 \tag{19}$$

2.3. Spatial discretization – the IsoGeometric formulation using NURBS

NURBS functions have been widely used because of their flexibility and computational efficiency, in several areas, such as computer graphics, FEM for solid/fluid mechanics and high-order differential equations, shape optimization, and time integration schemes (for instance, [26–30]).

In order to define the element concept in the context of IsoGeometric analysis, geometry, velocities, displacements, and displacement variations must be discretized with the following expressions:

$$\underline{\mathbf{x}}(\underline{\xi},t) = \sum_{a=1}^{n_{np}} R_a(\underline{\xi})\underline{\mathbf{x}}_a \qquad \underline{\mathbf{u}}(\underline{\xi},t) = \sum_{a=1}^{n_{np}} R_a(\underline{\xi})\underline{\mathbf{u}}_a$$
$$\underline{\ddot{\mathbf{u}}}(\underline{\xi},t) = \sum_{a=1}^{n_{np}} R_a(\underline{\xi})\underline{\ddot{\mathbf{u}}}_a \qquad \underline{\delta\mathbf{u}}(\underline{\xi},t) = \sum_{a=1}^{n_{np}} R_a(\underline{\xi})\underline{\delta\mathbf{u}}_a \tag{20}$$

where R_a is the NURBS basis function related to control point a, which is defined as function of the parametric coordinates (ξ,η,ζ), and n_{np} is the number of global control points (basis functions). Knot vectors corresponding to the different directions in the parametric space must be also specified, defining the non-zero knot spans where elements are then identified. A three-dimensional knot vector $(\Xi, \mathcal{H}, \mathcal{Z})$ may be written as follows:

$$\Xi(\xi) = \{\underbrace{0,\dots,0}_{p+1}, \xi_{p+1},\dots,\xi_{s_p-p-1}, \underbrace{1,\dots,1}_{p+1}\}, \text{ with } s_p = n+p+1$$
$$\mathcal{H}(\eta) = \{\underbrace{0,\dots,0}_{q+1}, \eta_{q+1},\dots,\eta_{s_q-q-1}, \underbrace{1,\dots,1}_{q+1}\}, \text{ with } s_q = m+q+1 \tag{21}$$
$$\mathcal{Z}(\zeta) = \{\underbrace{0,\dots,0}_{r+1}, \zeta_{r+1},\dots,\zeta_{s_r-r-1}, \underbrace{1,\dots,1}_{r+1}\}, \text{ with } s_r = l+r+1$$

where p, q, and r are the polynomial degrees of the basis functions over the parametric directions ξ, η, and ζ, respectively, and the corresponding numbers of basis functions are specified by $n + 1, m + 1$, and $l + 1$, respectively, which are also associated with the number of control points in the different directions of the physical space. Depending on the geometric topology of the problem, the knot vector may be reduced to two-dimensional or one-dimensional vectors, i.e., $(\Xi, \mathcal{H})$ or (Ξ).

The NURBS basis functions for three-dimensional applications are defined by

$$R_{i,j,k}^{p,q,r}(\xi, \eta, \zeta) = \frac{N_{i,p}(\xi)N_{j,q}(\eta)N_{k,r}(\zeta)w_{i,j,k}}{\sum\limits_{\hat{i},\hat{j},\hat{k}=0}^{n,m,l} N_{\hat{i},p}(\xi)N_{\hat{j},q}(\eta)N_{\hat{k},r}(\zeta)w_{\hat{i},\hat{j},\hat{k}}} \tag{22}$$

where the subscripts i, j, and k indicate the position of the control point in the index space and the superscripts p, q, and r define the polynomial degree of the basis functions. The weight term $w_{i,j,k}$ is related to the weight associated with the control point defined by the subindices i, j, and k. Details on evaluation of basis functions may be found in [31] and [32].

The Cox-de Boor recursive formulation [33, 34] is usually adopted to evaluate B-spline basis functions, which are obtained considering a given one-dimensional knot vector $\Xi(\xi)$ defined over the parametric space ξ, the number of control points defined along the corresponding direction in the physical space, and the polynomial order of the corresponding basis functions. According to the Cox-de Boor formulation, the B-spline basis functions may be expressed as

$$N_{i,0}(\xi) = \begin{cases} 1 & \text{if } \xi_i \leqslant \xi < \xi_{i+1}, \\ 0 & \text{otherwise.} \end{cases}$$
$$N_{i,p}(\xi) = \frac{\xi - \xi_i}{\xi_{i+p} - \xi_i} N_{i,p-1}(\xi) + \frac{\xi_{i+p+1} - \xi}{\xi_{i+p+1} - \xi_{i+1}} N_{i+1,p-1}(\xi) \tag{23}$$

where p is the polynomial degree of the basis function $N(\xi)$ and i is the knot index. Equation (23) is straightforwardly extended to the basis functions associated with the parametric directions η and ζ.

The IsoGeometric model for the equation of motion given by Equation (19) can be written as:

$$\int_{t_0}^{t} \bigcup_{e=1}^{n_{el}} \left(\int_{\Omega_e} \rho \underline{\delta \mathbf{u}} \cdot \underline{\ddot{\mathbf{u}}} \, d\Omega + \int_{\Omega_e} \underline{\delta \mathbf{u}} \cdot \chi \underline{\dot{\mathbf{u}}} \, d\Omega \right.$$
$$\left. - \int_{\Omega_e} \underline{\underline{\delta \boldsymbol{\epsilon}}} : \underline{\underline{\boldsymbol{\sigma}}} \, d\Omega + \int_{\Omega_e} \underline{\delta \mathbf{u}} \cdot \underline{\mathbf{b}} \, d\Omega + \int_{\Gamma_{Ne}} \underline{\delta \mathbf{u}} \cdot \underline{\mathbf{t}} \, d\Gamma \right) dt = 0 \tag{24}$$

where Ω_e and Γ_e are volume and boundary surfaces, respectively, corresponding to element e in the physical mesh. Considering $n + 1, m + 1$, and $l + 1$ as the number of basis functions related to the parametric directions ξ, η, and ζ, respectively, and their respective polynomial degrees denoted by p, q, and r, element e is defined by determining the indices at which the corresponding non-zero knot span begins in the index space, that is,

$$e \triangleq [\xi_i, \xi_{i+1}] \times [\eta_i, \eta_{i+1}] \times [\zeta_i, \zeta_{i+1}] \tag{25}$$

where $p+1 \leqslant i \leqslant n, q+1 \leqslant j \leqslant m$, and $r+1 \leqslant k \leqslant l$. The total number of elements at maximum continuity, n_{el}, in which the spatial field is discretized in the parametric domain is defined as

$$n_{el} = (n - p + 1) \cdot (m - q + 1) \cdot (l - r + 1) \tag{26}$$

By substituting the NURBS approximation related to the displacement field (Equation (20)) into the constitutive equation (Equation (2)), an element level approximation of the stress–strain relation, using Voigt notation, is obtained, where the strain components in the corotational system are given by

$$\hat{\boldsymbol{\epsilon}} = \hat{\mathbf{B}} \cdot \hat{\mathbf{u}} \tag{27}$$

where $\hat{\mathbf{B}}$ and $\hat{\mathbf{u}}$ are the symmetric part of the gradient operator and the displacements field, respectively, which are evaluated by referring to the current configuration of the body in the corotational

coordinate system. When infinitesimal displacements and rotations are observed, Equation (27) is described in terms of the undeformed configuration of the body (Ω_0). Derivatives of the B-spline basis functions are represented in terms of B-spline lower-order bases owing to the recursive definition of the basis functions. Algorithms for numerical evaluation of derivatives of B-spline basis functions may be found in [32].

Introducing the expansions shown in Equation (20) and the relationship given by Equation (27) into Equation (24), a matrix equation representing a system of algebraic equations is obtained for the equation of motion, which may be expressed as:

$$\bigcup_{e=1}^{n_{el}} \mathbf{M}^e \ddot{\mathbf{u}} + \bigcup_{e=1}^{n_{el}} \mathbf{C}^e \dot{\mathbf{u}} + \bigcup_{e=1}^{n_{el}} \mathbf{K}^e \mathbf{u} = \bigcup_{e=1}^{n_{el}} \mathbf{f}_{ext}^e \qquad (28)$$

where $\mathbf{M}^e$ and $\mathbf{K}^e$ are the element mass and element stiffness matrices, respectively, and $\mathbf{f}_{ext}^e$ is the force vector at element level. The matrix and vector dimensions associated to $\mathbf{M}^e$ and $\mathbf{K}^e$, and $\mathbf{f}_{ext}^e$, are specified as ($n_{eq} \times n_{eq}$) and (n_{eq}), respectively, where $n_{eq} = n_{en} \times n_{dof}$, with n_{dof} and $n_e n$ denoting the number of degrees of freedom at the control point level and the number of basis functions at the element level, respectively. The union symbol indicates the assembling procedure to evaluate the global system of equations, considering the element contributions given according to connectivity relations established among the control points. The global stiffness matrix is always sparse because the support of each basis function is highly localized.

In the geometrically nonlinear regime, the system of equations represented by Equation (28) must be iteratively satisfied using the incremental approach [35], because internal forces are given now as functions of the current configuration of the body. The nonlinear equation of motion is obtained by employing a linearization procedure given by the Newton–Raphson method, where the residual vector is submitted to a Taylor series expansion within the time interval $[t_n, t_{n+1}]$. Consequently, Equation (28) must be rewritten as follows:

$$\bigcup_{e=1}^{n_{el}} \mathbf{M}^e \ddot{\mathbf{u}} + \bigcup_{e=1}^{n_{el}} \mathbf{C}^e \dot{\mathbf{u}} + \bigcup_{e=1}^{n_{el}} \mathbf{K}_{tan}^e(\mathbf{u}^e)\Delta\mathbf{u} = \bigcup_{e=1}^{n_{el}} \mathbf{f}_{ext}^e - \bigcup_{e=1}^{n_{el}} \mathbf{f}_{int}^e(\mathbf{u}^e) \qquad (29)$$

where $\mathbf{K}_{tan}^e$ is the tangent stiffness matrix. At each iterative step, the tangent stiffness matrix and the internal force vector are initially evaluated in the corotational coordinate system with the following expressions:

$$\hat{\mathbf{K}}_{tan}^e = \int_{\hat{\Omega}^e} \hat{\mathbf{B}}^t \left(\hat{\mathbf{C}}^{mat} + \hat{\mathbf{C}}^{geo} \right) \hat{\mathbf{B}} \, \mathrm{d}\hat{\Omega}^e; \quad \hat{\mathbf{f}}_{int}^e = \int_{\hat{\Omega}^e} \hat{\mathbf{B}}^t \hat{\boldsymbol{\sigma}} \, \mathrm{d}\hat{\Omega}^e \qquad (30)$$

where $\hat{\Omega}^e$ is referenced to the current configuration of element e in the corotational coordinate system, and $\hat{\mathbf{C}}$ and $\hat{\boldsymbol{\sigma}}$ are stress tensors related to the Jaumann rate tensor and the corotational Cauchy stress tensor, respectively, with both evaluated in the corotational coordinate system. In order to solve the system of nonlinear equations of motion, the tangent stiffness matrix and the internal force vector must be obtained in the global coordinate system through an objective transformation from the corotational system, that is,

$$\mathbf{K}_{tan}^e = \mathbf{R}^t \hat{\mathbf{K}}_{tan}^e \mathbf{R}; \quad \mathbf{f}_{int}^e = \mathbf{R}^t \hat{\mathbf{f}}_{int}^e \qquad (31)$$

where $\mathbf{R}$ is the rotation matrix defined in the previous section. For additional information about solid NURBS and this numerical approach, the readers are addressed to [23].

2.4. Temporal integration – the generalized-α method and generalized energy–momentum method + ξ

The total time interval where the dynamic analysis is carried out $[t_0, t_f]$ is subdivided into time steps $\Delta t = t_{n+1} - t_n$ in order to define the time step in the integration process for implicit algorithms, where the incremental approach is adopted. The kinematic variables are assumed to be known at the beginning of every time step of the time integration, and the same variables are obtained at the

end of the respective time step considering the solution of the equation of motion, which is given in terms of displacement increments, and time approximations provided by a specific method, such as the Newmark's method. Although the Newmark's algorithm is unconditionally stable for linear problems, it may be unstable in the nonlinear range. In this sense, the $G\alpha$ method and GEMM+ξ may be utilized, where the equilibrium of the equation of motion is verified at an intermediate point of the time increment instead of the end point employed by the classical Newmark scheme.

It is assumed that $\mathbf{d}_{n+1} \approx \mathbf{u}(t_{n+1})$, $\mathbf{v}_{n+1} \approx \dot{\mathbf{u}}(t_{n+1})$, and $\mathbf{a}_{n+1} \approx \ddot{\mathbf{u}}(t_{n+1})$. At the beginning of each incremental step, the predictor phase is defined according to the Newmark's formulas

$$
\begin{aligned}
\mathbf{d}^i_{n+1} &= \tilde{\mathbf{d}}_{n+1} \\
\mathbf{v}^i_{n+1} &= \tilde{\mathbf{v}}_{n+1} \\
\mathbf{a}^i_{n+1} &= \tilde{\mathbf{a}}_{n+1}
\end{aligned}
\tag{32}
$$

where

$$
\tilde{\mathbf{d}}_{n+1} = \mathbf{d}_n + \Delta t \mathbf{v}_n + \frac{(\Delta t)^2}{2}\left((1 - 2\beta)\mathbf{a}_n + 2\beta\tilde{\mathbf{a}}_{n+1}\right)
\tag{33a}
$$

$$
\tilde{\mathbf{v}}_{n+1} = \mathbf{v}_n + \Delta t\left((1 - \gamma)\mathbf{a}_n + \gamma\tilde{\mathbf{a}}_{n+1}\right)
\tag{33b}
$$

The kinematic variables and residual of the governing equations are defined in the $G\alpha$ and GEMM+ξ by using the following functions:

$$
\mathbf{R}\left(\mathbf{d}_{n+\alpha_f}, \mathbf{v}_{n+\alpha_f}, \mathbf{a}_{n+\alpha_m}\right) = \mathbf{0}
\tag{34a}
$$

$$
\mathbf{d}_{n+\alpha_f} = \mathbf{d}_n + \alpha_f\left(\mathbf{d}_{n+1} - \mathbf{d}_n\right)
\tag{34b}
$$

$$
\mathbf{v}_{n+\alpha_f} = \mathbf{v}_n + \alpha_f\left(\mathbf{v}_{n+1} - \mathbf{v}_n\right)
\tag{34c}
$$

$$
\mathbf{a}_{n+\alpha_m} = \mathbf{a}_n + \alpha_m\left(\mathbf{a}_{n+1} - \mathbf{a}_n\right)
\tag{34d}
$$

$$
\text{with Newmark's formulas}
\tag{34e}
$$

The equilibrium, Equation (34a), must be satisfied at the intermediate level. Once $(\mathbf{d}_n, \mathbf{v}_n, \mathbf{a}_n)$ is known, $\left(\mathbf{d}_{n+1}, \mathbf{v}_{n+1}, \mathbf{a}_{n+1}, \mathbf{d}_{n+\alpha_f}, \mathbf{v}_{n+\alpha_f}, \mathbf{a}_{n+\alpha_m}\right)$ can be obtained, where $\alpha_f, \alpha_m, \gamma$, and β are parameters defining the method, which are selected in order to achieve second-order accuracy and unconditional stability.

According to [5], second-order accuracy and unconditional stability may be obtained for second-order linear differential equations with constant coefficients by using

$$
\gamma = \frac{1}{2} - \alpha_f + \alpha_m
\tag{35a}
$$

$$
\beta = \frac{1}{4}(1 - \alpha_f + \alpha_m)^2
\tag{35b}
$$

In order to obtain a numerical scheme with controllable numerical damping over the high frequencies, α_m and α_f must be defined as functions of spectral radius ρ_∞. In [5], it is established that, for system with second-order accuracy, one obtains

$$
\alpha_m = \frac{2 - \rho^c_\infty}{1 + \rho^c_\infty}
\tag{36a}
$$

$$
\alpha_f = \frac{1}{1 + \rho^c_\infty}
\tag{36b}
$$

There is an additional dissipation parameter in the GEMM+ξ that displaces the internal force of the intermediate level defined by $G\alpha$, from $t_{n+\alpha_f} \rightarrow t_{n+\alpha+\xi}$. This parameter, which is known as the Armero–Petocz parameter [18], improves stability and is given by

$$
\xi = \frac{1 - \rho_\infty}{2 + 2\rho_\infty}
\tag{37}
$$

Assuming that the strain and stress tensors and all kinematical quantities are known at the end of the last time increment $t = t_n$, the solution at $t = t_{n+1}$ should be computed based on the converged

solution at the previous time step. An algorithm describing all the calculation steps performed by the present numerical model is found in the succeeding text.

1. **Predictor Phase**:

   select a predictor according to the Newmark's formulas estimating $\left(\mathbf{d}_{n+1}^0, \mathbf{v}_{n+1}^0, \mathbf{a}_{n+1}^0\right)$

   $$\text{(38)}$$

2. **Corrector Phase**: loop over $i = 0, \ldots, i_{max}$

   (a) evaluate $\left(\mathbf{d}_{n+\alpha_f}^i, \mathbf{v}_{n+\alpha_f}^i, \mathbf{a}_{n+\alpha_m}^i\right)$

   $$\mathbf{d}_{n+\alpha_f}^i = (1 - \alpha_f)\mathbf{d}_n + \alpha_f \mathbf{d}_{n+1}^i \tag{39a}$$

   $$\mathbf{v}_{n+\alpha_f}^i = (1 - \alpha_f)\mathbf{v}_n + \alpha_f \mathbf{v}_{n+1}^i \tag{39b}$$

   $$\mathbf{a}_{n+\alpha_m}^i = (1 - \alpha_m)\mathbf{a}_n + \alpha_m \mathbf{a}_{n+1}^i \tag{39c}$$

   (b) Assembly the residual vector with variables at the intermediate level

   $$\frac{d\mathbf{R}^i}{d\mathbf{d}_{n+1}}\Delta\mathbf{d} = -\mathbf{R}_{n+1}^i \tag{40}$$

   where

   $$\mathbf{R}_{n+1}^i = \mathbf{R}\left(\mathbf{d}_{n+\alpha_f}^i, \mathbf{v}_{n+\alpha_f}^i, \mathbf{a}_{n+\alpha_m}^i\right)$$
   $$^{\text{G}\alpha}\mathbf{R}_{n+1}^i = \mathbf{Ma}_{n+\alpha_m}^i + \mathbf{Cv}_{n+\alpha_f}^i + {}^{\text{G}\alpha}\mathbf{N}_{n+\alpha_f}^i - \mathbf{f}_{n+\alpha_f}^{ext} \tag{41}$$
   $$^{\text{GEMM}+\xi}\mathbf{R}_{n+1}^i = \mathbf{Ma}_{n+\alpha_m}^i + \mathbf{Cv}_{n+\alpha_f}^i + {}^{\text{GEMM}+\xi}\mathbf{N}_{n+\alpha_f+\xi}^i - \mathbf{f}_{n+\alpha_f}^{ext}$$

   $\mathbf{N}$ is the internal force vector and $\mathbf{f}_{n+\alpha_f}^{ext} = (1 - \alpha_f)\mathbf{f}_n^{ext} + \alpha_f \mathbf{f}_{n+1}^{ext}$ is the external load vector evaluated at generalized intermediate point. The following expression

   $$\frac{d\mathbf{R}^i}{d\mathbf{d}_{n+1}} = \frac{d\mathbf{R}}{d\mathbf{d}_{n+1}}\left(\mathbf{d}_{n+\alpha_f}^i, \mathbf{v}_{n+\alpha_f}^i, \mathbf{a}_{n+\alpha_m}^i\right) \tag{42}$$

   is the total derivative $\left(\frac{d\mathbf{R}}{d\mathbf{d}_{n+1}}\right)$, which is presented in Equations (44) and (45).

   (c) with the solution of Equation (40), kinematic variables are updated

   $$\mathbf{d}_{n+1}^{i+1} = \mathbf{d}_{n+1}^i + \Delta\mathbf{d}$$
   $$\mathbf{v}_{n+1}^{i+1} = \mathbf{v}_{n+1}^i + \frac{\gamma}{\beta\Delta t}\Delta\mathbf{d} \tag{43}$$
   $$\mathbf{a}_{n+1}^{i+1} = \mathbf{a}_{n+1}^i + \frac{1}{\beta(\Delta t)^2}\Delta\mathbf{d}$$

3. **Check convergence**: If the criterion is not satisfied, return to step 1, with $i = i + 1$. Otherwise, go forward to the next time step.

The total derivative of Equation (42) is obtained as follows:

$$\frac{d\mathbf{R}}{d\mathbf{d}_{n+1}} = \frac{d\mathbf{R}}{d\mathbf{d}_{n+\alpha_f}}\frac{d\mathbf{d}_{n+\alpha_f}}{d\mathbf{d}_{n+1}}$$
$$+ \frac{d\mathbf{R}}{d\mathbf{v}_{n+\alpha_f}}\frac{d\mathbf{v}_{n+\alpha_f}}{d\mathbf{v}_{n+1}}\frac{d\mathbf{v}_{n+1}}{d\mathbf{d}_{n+1}} \tag{44}$$
$$+ \frac{d\mathbf{R}}{d\mathbf{a}_{n+\alpha_m}}\frac{d\mathbf{a}_{n+\alpha_m}}{d\mathbf{a}_{n+1}}\frac{d\mathbf{a}_{n+1}}{d\mathbf{d}_{n+1}}$$

And from Equations (33) and (38), one obtains

$$\frac{d\mathbf{R}}{d\mathbf{d}_{n+1}} = \frac{\alpha_m}{\beta(\Delta t)^2}\mathbf{M} + \frac{\gamma\alpha_f}{\beta\Delta t}\mathbf{C} + \mathbf{K}_{tan} \tag{45}$$

In Gα method, the internal force and tangent stiffness matrix at generalized intermediate point are evaluated according to the following expression:

$$^{G\alpha}\mathbf{N}^i_{n+\alpha_f} = (1-\alpha_f)\int_{\hat{\Omega}} \hat{\mathbf{B}}^t(\hat{\mathbf{u}}_n)\,\hat{\sigma}(\hat{\mathbf{u}}_n)\,d\hat{\Omega} + \alpha_f\int_{\hat{\Omega}} \hat{\mathbf{B}}^t(\hat{\mathbf{u}}_{n+1})\,\hat{\sigma}(\hat{\mathbf{u}}_{n+1})\,d\hat{\Omega} \tag{46}$$

$$\begin{aligned}
^{G\alpha}\mathbf{K}^{tan}_{n+\alpha_f} &= \alpha_f(\mathbf{K}_{mat} + \mathbf{K}_{geo}) \\
&= \alpha_f\int_{\hat{\Omega}} \hat{\mathbf{B}}^t(\hat{\mathbf{u}}_{n+1})\left(\hat{\mathbf{C}}^{mat} + \hat{\mathbf{C}}^{geo}(\hat{\mathbf{u}}_{n+1})\right)\hat{\mathbf{B}}(\hat{\mathbf{u}}_{n+1})\,d\hat{\Omega}
\end{aligned} \tag{47}$$

while in GEMM+ξ, the internal force and tangent stiffness matrix at generalized intermediate point are evaluated according to the following expression:

$$^{GEMM+\xi}\mathbf{N}^i_{n+\alpha_f+\xi} = \int_{\hat{\Omega}} \hat{\mathbf{B}}^t(\hat{\mathbf{u}}_{n+\alpha_f})\left[(\alpha_f-\xi)\hat{\sigma}(\hat{\mathbf{u}}_n) + (\alpha_f+\xi)\hat{\sigma}(\hat{\mathbf{u}}_{n+1})\right]d\hat{\Omega} \tag{48}$$

$$\begin{aligned}
^{GEMM+\xi}\mathbf{K}^{tan}_{n+\alpha_f+\xi} &= (\alpha_f+\xi)\mathbf{K}_{mat} + \alpha_f\mathbf{K}_{geo} \\
&= (\alpha_f+\xi)\int_{\hat{\Omega}} \hat{\mathbf{B}}^t(\hat{\mathbf{u}}_{n+\alpha_f})\,\hat{\mathbf{C}}^{mat}\hat{\mathbf{B}}(\hat{\mathbf{u}}_{n+1})\,d\hat{\Omega} \\
&\quad + \alpha_f\int_{\hat{\Omega}} \hat{\mathbf{B}}^t(\hat{\mathbf{u}}_{n+\alpha_f})\,\hat{\mathbf{C}}^{geo}(\hat{\mathbf{u}}_{n+\alpha_f})\,\hat{\mathbf{B}}(\hat{\mathbf{u}}_{n+\alpha_f})\,d\hat{\Omega} \\
&\approx (\alpha_f+\xi)\int_{\hat{\Omega}} \hat{\mathbf{B}}^t(\hat{\mathbf{u}}_{n+\alpha_f})\,\hat{\mathbf{C}}^{mat}\hat{\mathbf{B}}(\hat{\mathbf{u}}_{n+\alpha_f})\,d\hat{\Omega} \\
&\quad + \alpha_f\int_{\hat{\Omega}} \hat{\mathbf{B}}^t(\hat{\mathbf{u}}_{n+\alpha_f})\,\hat{\mathbf{C}}^{geo}(\hat{\mathbf{u}}_{n+\alpha_f})\,\hat{\mathbf{B}}(\hat{\mathbf{u}}_{n+\alpha_f})\,d\hat{\Omega}
\end{aligned} \tag{49}$$

It is important to notice that material contribution into tangent stiffness matrix is modified in order to get a symmetry matrix.

Regarding the applications carried out, the convergence criteria adopted here determine that the maximum tolerance is $2 \cdot 10^{-8}$.

The in-house code GNUall was developed for this work (based on libraries GNUiga and GNUrbs) using FORTRAN (IBM, Armonk, NY, USA).

2.5. Total energy, and linear and angular momentum

There are some quantities that have a great importance in structural dynamics, such as total energy, and linear and angular momentum, in order to judge the stability and conservative properties. The total energy E is composed by kinetic energy K and internal strain energy U

$$E = K + U \tag{50a}$$

$$K = \frac{1}{2}\int_{\Omega} \rho\underline{\dot{\mathbf{u}}} \cdot \underline{\dot{\mathbf{u}}}\,d\Omega \tag{50b}$$

$$U = \frac{1}{2}\int_{\Omega} \underline{\underline{\sigma}} : \underline{\underline{\epsilon}}\,d\Omega \tag{50c}$$

The linear and angular momentum can be evaluated as

$$\underline{\mathbf{L}} = \int_{\Omega} \rho\underline{\dot{\mathbf{u}}}\,d\Omega \tag{51a}$$

$$\underline{\mathbf{J}} = \int_{\Omega} \rho\underline{\mathbf{u}} \times \underline{\dot{\mathbf{u}}}\,d\Omega \tag{51b}$$

3. NUMERICAL APPLICATIONS

In the numerical examples, independent of the continuity class only single patches are used. It is worth noting that for the cylindrical shell (example 3.5) a NURBS description is used, while a B-spline is employed in the other examples.

The concept of *hpk*-refinement was introduced in [31], and several examples have shown that a high continuity improves the accuracy, specially in the longitudinal vibration problem 3.1. Unlike the classical *k*-refinement, where the continuity is increased together with the degree (like a *pk*-refinement), one can increase the continuity together with the number of elements (like an *hk*-refinement) without changing the polynomial degree. Therefore, one can increase the continuity until a desired order, i.e., between C^0 to C^{p-k}, being p the degree and k the knot multiplicity. In this work, the first three numerical examples are carried out using a fixed degree (quintic-NURBS) in the space discretization, while the continuity class is increased from zero to four, keeping constant the number of degrees of freedom. Finally, with this procedure only 'h' and 'k' are refined. On the other hand, in the last example only two continuity are employed, C^1 and C^4, wherein the first one has a mesh more refined, i.e., $8 \times 8C^1$ elements in the shell surface, while only $4 \times 4C^4$ elements in the second mesh are used.

In order to evaluate the numerical dissipation, the following expression is used: $\frac{W-E}{W}\%$, where W is the external work and E is the total energy.

3.1. Dispersion analysis in longitudinal vibrations of an elastic rod: the Helmholtz equation

In order to be brief and concise, as a complement of the work presented in [31], a dispersion analysis of the longitudinal vibrations of a rod is carried out. These results may be valuable to explain how the continuity class can improve both the numerical stability and the energy–momentum conservation. For additional information about the physical problem and the analytical solution, readers are addressed to [31].

The classical linear scalar equation governing longitudinal vibrations of a rod is given by

$$E\nabla^2 u - \rho\ddot{u} = 0 \tag{52}$$

being E, ρ, and u the constant Young's modulus, density per unit length, and the longitudinal displacement, respectively. Assuming time-harmonic solutions, the following equation (continuous eigenproblem) is obtained:

$$E\nabla^2 u - \rho\,\omega^2 u = 0 \tag{53}$$

where ω is the natural frequency.

The continuum problem has infinite nontrivial solutions. The discrete problem can be written as a generalized eigenproblem as follows:

$$\left(\mathbf{K} - \left(\omega_i^h\right)^2 \mathbf{M}\right)\phi_i = \mathbf{0} \tag{54}$$

where homogeneous Dirichlet boundary conditions are employed. ω_i^h and ϕ_i are the i-th eigen pair, eigenvalue and eigenvector, respectively.

The frequencies ω_n^h numerically obtained (being $N = 666$ the total number of degrees of freedom) are compared with the theoretical ones, $\omega_n = n\pi$, $n = 1, \ldots, N$. Therefore, the curve $\omega^h/\omega = 1$ means that the exact solution is obtained. In particular, in Figure 1(a), *pk*-refinement and *p*-refinement are presented from $p = 1(C^0)$ up to $p = 5(C^4)$, while in Figure 1(b) for a fixed quintic-NURBS basis, the continuity class is elevated from C^0 up to C^4, like an *hk*-refinement. ω^h/ω with larger values indicates decreased accuracy. From Figure 1(a), it is observed that by increasing p the accuracy of the lower frequencies are improved while the accuracy of the higher ones are deteriorated. Unlike *p*-refinement, *pk*-refinement improves both ranges, lower and higher frequencies. On the other hand, *hk*-refinement shows a similar behavior, i.e., by increasing the number of elements and the continuity of the basis functions, all frequencies are more close to the theoretical ones.
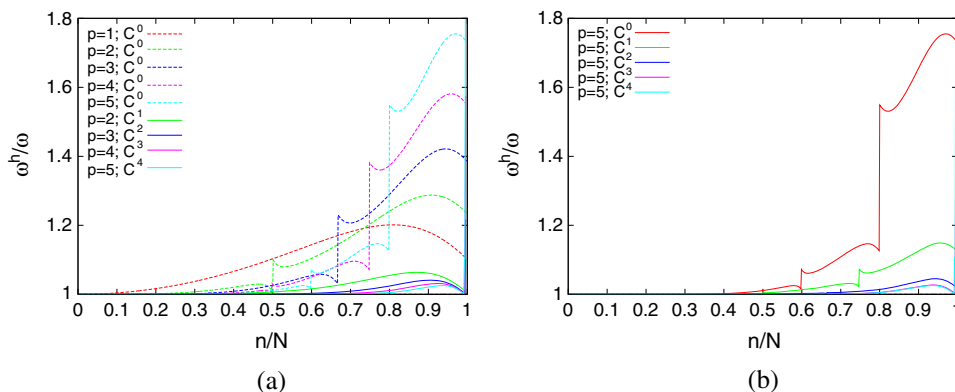
Figure 1. The continuity influences on the eigenproblem. (a) *p*-refinement and *pk*-refinement; and (b) *hk*-refinement.

By increasing p, strange frequencies at the very end of the spectrum are observed, as noticed in [31], referred to as 'outlier frequencies', whose number and magnitude increase with p.

Higher frequencies and ill-resolved higher modes are the main triggers to yield numerical instability. Using as a baseline this linear problem, one can expect that when higher frequencies are more accurate, the more stable will be the nonlinear case. Furthermore, considering that $\omega_i^h > \omega_i$, this difference is increased when a low continuity is adopted. Any controllable dissipative time integrator will exhibit less numerical damping over higher frequencies if higher continuity is used. Therefore, an improvement is expected when higher continuity is employed.

3.2. Clamped beam

A cantilever beam subject to pressure loading and undergoing large displacements is analyzed in this example, where plane strain state is also assumed. This dynamic problem was proposed by Bathe and Baig [36] to show the time integration failure in Newmark's method.

Geometry and boundary conditions are shown in Figure 2(a), while load description is presented in Figure 2(b). Material properties of the structure as well as the time step adopted in the time integration procedure are found in Table I. Information on computational parameters used in the set of numerical analyses carried out here, which correspond to the IsoGeometric formulation and the time discretization scheme proposed in this work, are summarized in Table II. Number and distribution ($L \times h \times w$) of elements over the physical space referring to the cantilever beam are
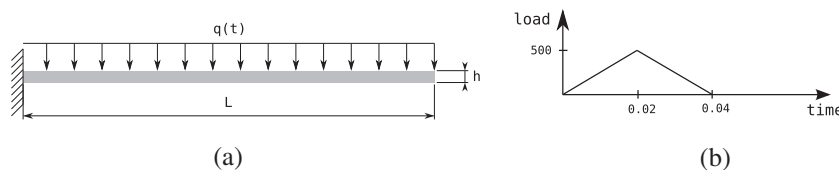

Figure 2. Geometry, boundary condition, and load description for the clamped beam: $L = 0.4$ m; $h = 0.001$ m. (a) Geometry and boundary conditions; and (b) load $q(t)$.

Table I. Geometrical and load characteristics for the cantilever beam analysis.

Young modulus	E (N/m^2)	$7 \cdot 10^{10}$
Poisson coefficient	ν	0.25
Specific mass	ρ (kg/m^3)	$2.7 \cdot 10^3$
Damping coefficient	ϕ	0.0
Time step	Δt (s)	$4.0 \cdot 10^{-3}$

Table II. Computational parameters employed in the cantilever beam analysis.

Control mesh	Number of elements	Continuity class	Spectral radius − ρ_∞	Degrees (p, q, r)
		Gα		
$66 \times 3 \times 2$	$13 \times 1 \times 1$	C^0	0.95; 0.99; 1.00*	5, 2, 1
$66 \times 3 \times 2$	$16 \times 1 \times 1$	C^1	0.95; 0.99; 1.00*	5, 2, 1
$66 \times 3 \times 2$	$21 \times 1 \times 1$	C^2	0.95; 0.99; 1.00*	5, 2, 1
$66 \times 3 \times 2$	$31 \times 1 \times 1$	C^3	0.95; 0.99; 1.00*	5, 2, 1
$66 \times 3 \times 2$	$61 \times 1 \times 1$	C^4	0.95; 0.99; 1.00*	5, 2, 1
		GEMM+ξ		
$66 \times 3 \times 2$	$13 \times 1 \times 1$	C^0	0.99; 1.00*	5, 2, 1
$66 \times 3 \times 2$	$16 \times 1 \times 1$	C^1	0.99; 1.00*	5, 2, 1
$66 \times 3 \times 2$	$21 \times 1 \times 1$	C^2	0.99; 1.00*	5, 2, 1
$66 \times 3 \times 2$	$31 \times 1 \times 1$	C^3	0.99; 1.00*	5, 2, 1
$66 \times 3 \times 2$	$61 \times 1 \times 1$	C^4	0.99; 1.00*	5, 2, 1

$(\cdot)^* \rightarrow$ simulations carried out with both consistent and lumped mass.

Gα, generalized-α; GEMM+ξ, generalized energy–momentum method + ξ.
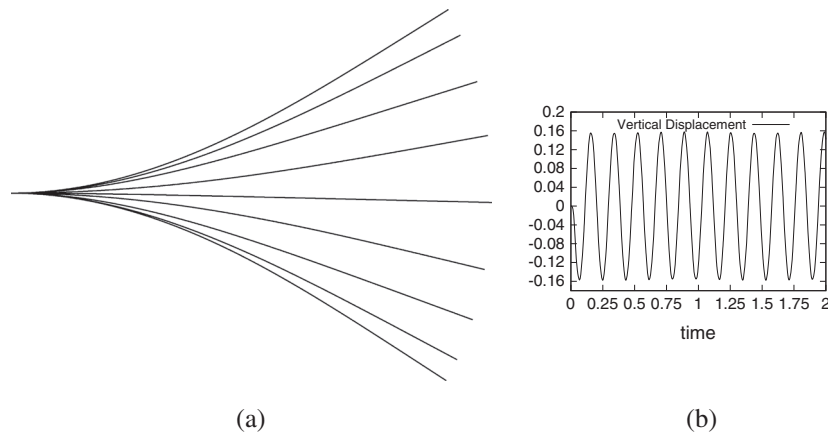

Figure 3. Generalized α with $\rho_\infty = 0.95$ and C^4. (a) Successive configurations and (b) tip vertical displacement.

given according to the continuity class, where the element configurations $(13 \times 1 \times 1), (16 \times 1 \times 1), (21 \times 1 \times 1), (31 \times 1 \times 1)$, and $(61 \times 1 \times 1)$ correspond to the continuity classes C^0, C^1, C^2, C^3, and C^4, respectively. In each simulation, the same number of degrees of freedom is used.

The motion of the cantilever beam performed during the period of oscillation [0.07 s, 0.15 s] can be visualized with $\Delta t = 0.01$ s in Figure 3(a), while in Figure 3(b), the result in terms of vertical displacements evaluated at the tip of the cantilever beam during the numerical simulation is presented using Gα with consistent mass, $\rho_\infty = 0.95$, and C^4. The time histories referring to the energy budget during the numerical simulation, obtained when consistent mass is employed, are shown in Figures 4 and 5 for Gα method and GEMM+ξ, respectively.

In order to evaluate the amount of numerical dissipation, several spectral radii are investigated using continuity class from zero to four. In Table III, the time-to-failure in the time integration shows that a stable analysis is obtained only for $\rho_\infty = 0.95$ and $\rho_\infty = 0.99$ for Gα method and GEMM+ξ, respectively, for the adopted time step. Although it is possible to obtain a stable analysis if a small time step is used, numerical instability allows understanding if there is influence of continuity class over the time integration algorithm, for both features of interest, numerical stability and energy conservation.
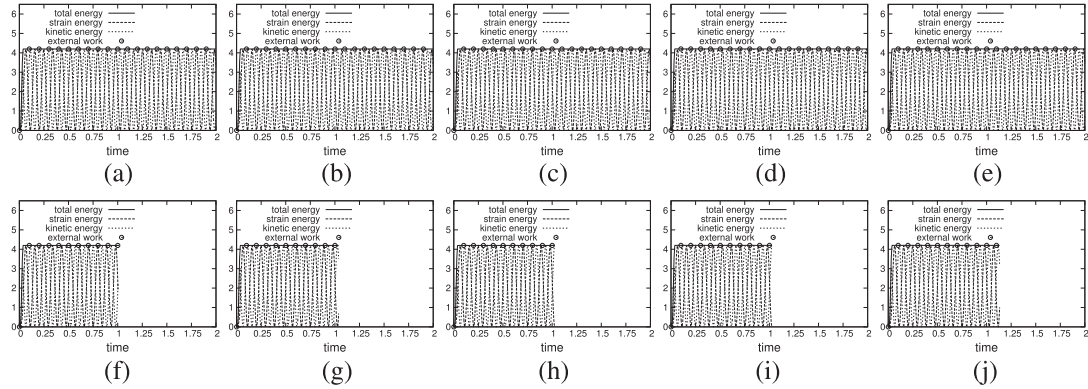
Figure 4. Energy of the clamped beam and generalized α with consistent mass. (a) $\rho_\infty = 0.95, C^0$; (b) $\rho_\infty = 0.95, C^1$; (c) $\rho_\infty = 0.95, C^2$; (d) $\rho_\infty = 0.95, C^3$; (e) $\rho_\infty = 0.95, C^4$; (f) $\rho_\infty = 1.00, C^0$; (g) $\rho_\infty = 1.00, C^1$; (h) $\rho_\infty = 1.00, C^2$; and (i) $\rho_\infty = 1.00, C^3$; (j) $\rho_\infty = 1.00, C^4$.
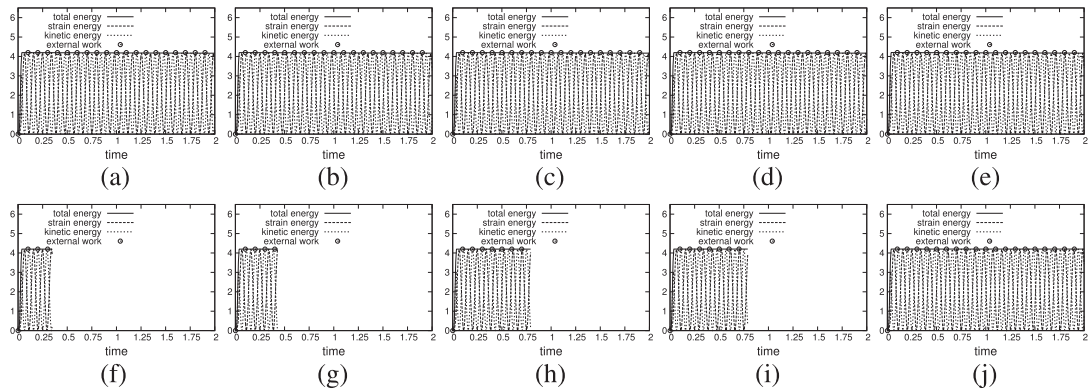

Figure 5. Energy of the clamped beam and generalized energy–momentum method $+\xi$ with consistent mass. (a) $\rho_\infty = 0.99, C^0$; (b) $\rho_\infty = 0.99, C^1$; (c) $\rho_\infty = 0.99, C^2$; (d) $\rho_\infty = 0.99, C^3$; (e) $\rho_\infty = 0.99, C^4$; (f) $\rho_\infty = 1.00, C^0$; (g) $\rho_\infty = 1.00, C^1$; (h) $\rho_\infty = 1.00, C^2$; (i) $\rho_\infty = 1.00, C^3$; and (j) $\rho_\infty = 1.00, C^4$.

In Table III, the percentages of numerical dissipation together with time-to-failure (placed in parentheses in the table) are presented. It is possible to notice that there is a dependence between the continuity class and the numerical instability. Although this dependence is non-monotonic, it seems that the instability is postponed when the continuity class is elevated. Indeed, this behavior is evident when GEMM+ξ with consistent mass is employed. On the other hand, the instability seems to be indifferent in front of continuity class for Gα method.

The present results demonstrate that the time integration process is suddenly interrupted when the amount of numerical dissipation is insufficient or non-existent ($\rho_\infty = 1.00$), unlike the finite element predictions obtained in [14], where numerical instabilities are clearly identified from the typical increase observed in the energy response. It is important to notice that in [14] a finite element formulation for eight-node hexahedral elements with one-point quadrature techniques was adopted. Also, in the analyses presented in [36], [9], and [17], it is always possible to identify a numerical instability once an oscillation is observed in the energy budget. It is also observed that the range of spectral radius with stable responses is significantly enlarged when results obtained considering the IsoGeometric formulation proposed in this work are compared with those obtained in [14] ($\rho_\infty < 0.3$). The displacement responses referring to $\rho_\infty = 0.95$ and $\rho_\infty = 0.99$ for Gα method and GEMM+ξ are in perfect agreement with numerical predictions presented in [36].

Some important features may be pointed out from this example. First, the total energy is conserved within a very small tolerance, independently of the spectral radius, time integrator, mass description,

Table III. Maximum level of the dissipation at the end of each analysis and time-to-failure (Section 3.2).

ρ_∞	C^0	C^1	C^2	C^3	C^4
			$G\alpha$ with consistent mass		
0.95	$3\cdot10^{-4}\%$	$2\cdot10^{-4}\%$	$2\cdot10^{-4}\%$	$2\cdot10^{-4}\%$	$2\cdot10^{-4}\%$
0.99	$6\cdot10^{-4}\%$ (1.74)	$\uparrow 3\cdot10^{-2}\%$ (1.21)	$4\cdot10^{-3}\%$ (1.56)	$1\cdot10^{-2}\%$ (1.79)	$8\cdot10^{-4}\%$ (1.69)
1.00	$4\cdot10^{-6}\%$ (1.01)	$1\cdot10^{-3}\%$ (1.04)	$\uparrow 1\cdot10^{-4}\%$ (1.02)	$\uparrow 3\cdot10^{-4}\%$ (1.03)	$\uparrow 6\cdot10^{-4}\%$ (1.13)
			$G\alpha$ with lumped mass		
1.00	0.018% (1.08)	0.25% (1.14)	0.11% (1.18)	0.12% (1.21)	0.066% (1.22)
			GEMM+ξ consistent mass		
0.99	0.71%	0.71%	0.71%	0.71%	0.71%
1.00	$5\cdot10^{-3}\%$ (0.35)	$\uparrow 3\cdot10^{-3}\%$ (0.43)	$\uparrow 4\cdot10^{-3}\%$ (0.79)	$\uparrow 4\cdot10^{-3}\%$ (0.79)	$3\cdot10^{-3}\%$
			GEMM+ξ lumped mass		
1.00	$1\cdot10^{-2}\%$ (1.81)	$2\cdot10^{-4}\%$ (0.97)	$5\cdot10^{-4}\%$ (0.97)	$2\cdot10^{-2}\%$	$4\cdot10^{-4}\%$ (1.89)
		$\uparrow$ implies in the growing of the total energy.			
		$(t_f) \rightarrow$ time-to-failure in seconds.			

$G\alpha$, generalized-α; GEMM+ξ, generalized energy–momentum method + ξ.

and continuity class. Naturally, for both time integrators, the lumped mass shows a greater amount of dissipation, as expected, and there is not a deterioration of the solution. Concerning the numerical stability, as expected, by increasing the numerical dissipation (once the spectral radius is decreased) a stable analysis is obtained. However, the most important result may be observed when GEMM+ξ with consistent mass is employed, i.e., the numerical instability is postponed, increasing the continuity class. This effect is not observed with $G\alpha$ with lumped or consistent mass nor for GEMM+ξ with lumped mass.

It was observed that the convergence rate in terms of displacement and force has not any dependence on the continuity class. Also, it was observed that the convergence rate of this analysis is about 2.2 for both force and displacement in $G\alpha$ method, while in GEMM+ξ, convergence rates about 1.8 and 1.6 for force and displacement, respectively, are observed. The convergence rate itself is indifferent when consistent or lumped mass is used.

The energy budget are shown in Figures 13 and 14 using consistent mass for $G\alpha$ and GEMM+ξ, respectively.

3.3. Toss rule – plane movement

This problem was studied in [9], where different time integration schemes are employed to understand the numerical dissipation and its stability. A numerical investigation of the plane movement of a toss rule is performed in this example, where a geometrically nonlinear dynamic analysis is carried out.

Geometry and boundary conditions are shown in Figure 6(a), while load description is presented in Figure 6(b). Material properties of the structure as well as the time step adopted in the time integration procedure are found in Table IV. It is important to notice that distributed loads are applied to the structure to produce the plane motion of the rule, which is free to fly in the absence of displacement constraint and gravity action. Computational parameters regarding the numerical analyses performed here are presented in Table V. Number and distribution (L, h, w) of elements over the physical space referring to the rule are again given according to the continuity class, where the element configurations $(13 \times 1 \times 1)$, $(16 \times 1 \times 1)$, $(21 \times 1 \times 1)$, $(31 \times 1 \times 1)$, and $(61 \times 1 \times 1)$ correspond to the continuity classes C^0, C^1, C^2, C^3, and C^4, respectively. In each simulation, the same number of degrees of freedom is used.
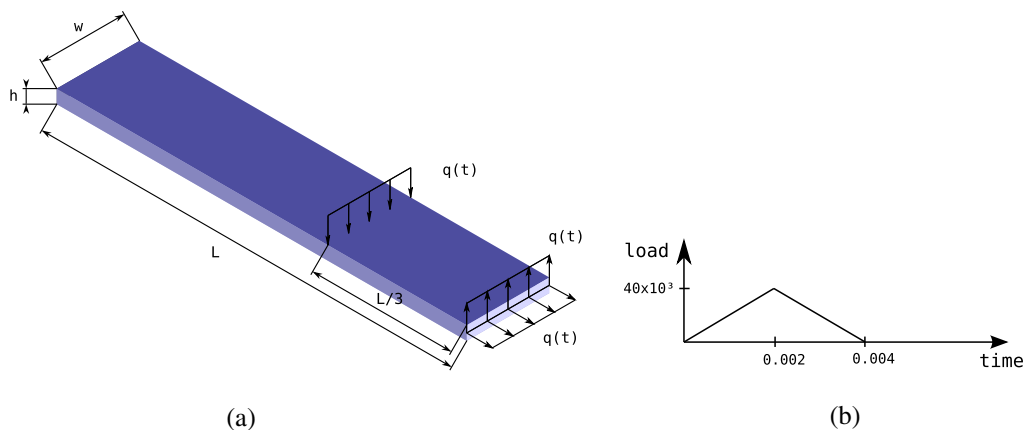
Figure 6. Geometry and boundary conditions of the toss rule: $L = 0.3$ m; $h = 0.002$ m; and $w = 0.06$ m. (a) Geometry and boundary conditions; and (b) load $q(t)$.

Table IV. Geometrical and load characteristics for the toss rule analysis.

Young modulus	E (N/m^2)	$2.06 \cdot 10^{11}$
Poisson coefficient	ν	0.3
Specific mass	ρ (kg/m^3)	$7.8 \cdot 10^3$
Damping coefficient	ϕ	0.0
Time step	Δt (s)	$1.0 \cdot 10^{-4}$

Table V. Computational parameters employed in the toss rule analysis.

Control mesh	Number of elements	Continuity class	Spectral radius – ρ_∞	Degrees (p, q, r)
		Gα		
$66 \times 3 \times 2$	$13 \times 1 \times 1$	C^0	$0.50; 0.95; 0.99; 1.00^*$	5, 2, 1
$66 \times 3 \times 2$	$16 \times 1 \times 1$	C^1	$0.50; 0.95; 0.99; 1.00^*$	5, 2, 1
$66 \times 3 \times 2$	$21 \times 1 \times 1$	C^2	$0.50; 0.95; 0.99; 1.00^*$	5, 2, 1
$66 \times 3 \times 2$	$31 \times 1 \times 1$	C^3	$0.50; 0.95; 0.99; 1.00^*$	5, 2, 1
$66 \times 3 \times 2$	$61 \times 1 \times 1$	C^4	$0.50; 0.95; 0.99; 1.00^*$	5, 2, 1
		GEMM+ξ		
$66 \times 3 \times 2$	$13 \times 1 \times 1$	C^0	1.00^*	5, 2, 1
$66 \times 3 \times 2$	$16 \times 1 \times 1$	C^1	1.00^*	5, 2, 1
$66 \times 3 \times 2$	$21 \times 1 \times 1$	C^2	1.00^*	5, 2, 1
$66 \times 3 \times 2$	$31 \times 1 \times 1$	C^3	1.00^*	5, 2, 1
$66 \times 3 \times 2$	$61 \times 1 \times 1$	C^4	1.00^*	5, 2, 1

$(\cdot)^* \rightarrow$ simulations carried out with both consistent and lumped mass.

Gα, generalized-α; GEMM+ξ, generalized energy–momentum method + ξ.

The dynamic responses obtained from the numerical analyses performed here are shown in Figure 7 for GEMM+ξ with consistent mass, $\rho_\infty = 1.00$, and C^4. Successive configurations are presented in Figure 7(a) and (b) in the intervals [0.01 s, 0.1 s] with $\Delta t = 0.01$ s and [0.001 s, 0.03 s] with $\Delta t = 0.001$ s, respectively. Linear and angular momentum are also presented in Figure 7(c).

Results shown here demonstrate again a sudden interruption of the time integration process when a spectral radius equal to $\rho_\infty = 1.00$ is considered (no numerical dissipation), independently of the continuity class used, for Gα method with consistent mass, whereas for lumped mass the

(a)

(b)

(c)

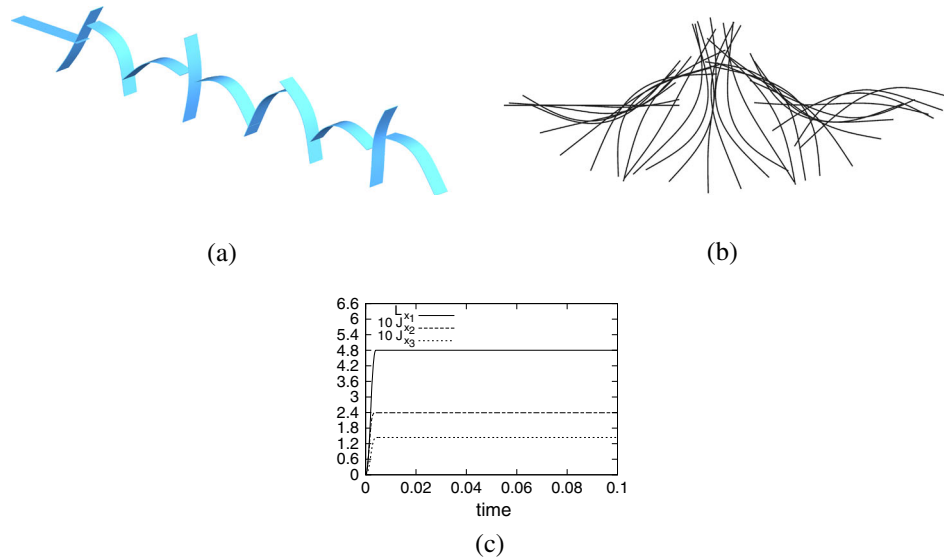Figure 7. Successive configurations: generalized energy–momentum method + ξ with $\rho_\infty = 1.00$ and C^4. (a) Spatial view; (b) plane view; and (c) linear and angular momentum, $\underline{\mathbf{L}}$ and $\underline{\mathbf{J}}$.

convergence is reached only for C^1 and C^2, and with the increase of continuity the numerical instability is anticipated. In this sense, the influence of the continuity class on the energy response was not identified for consistent mass. On the other hand, stable solutions can be obtained even with small amounts of numerical dissipation, i.e., $\rho_\infty = 0.99$, where the total energy is perfectly maintained (within a very small tolerance) during the total time interval of the numerical analysis. The same behavior was observed for the components of the angular and linear momentum. For analyses carried out with GEMM+ξ using consistent as well as lumped mass, stable analysis with the conservation of the energy and momentum is achieved. The range of stable spectral radius obtained with the IsoGeometric model is slightly wider than that presented by the finite element model proposed in [14]. Responses obtained here are in agreement with the numerical predictions presented in [9].

In Table VI, the numerical dissipation at the end of each analysis and the time-to-failure are presented. It is observed that there is not a dependence between the conservation of the total energy and linear, angular momentum on the continuity class. On the other hand, the stability shows a different behavior with respect to the first example. For Gα with consistent mass, there is not a dependence between the stability and the continuity class, while for Gα with lumped mass, it seems that the instability is postponed when the continuity class is reduced.

In [9], [16], and [17], a parametric study is carried out as function of spectral radius for several time integration methods, such as constrained energy–momentum method [9], energy–momentum method, GEMM [17], modified energy–momentum method, and Gα method. Unlike results obtained here with NURBS basis functions, for any time integrator scheme, it is possible to see a deterioration of the solution in terms of energy budget and momentum conservation with the increase of the spectral radius.

It was observed that the convergence rates of this analysis are about 1.9 and 2.1 for force and displacement convergence, respectively, in Gα method, while in GEMM+ξ, convergence rates about 1.7 and 1.9 for force and displacement convergence, respectively, are observed. The convergence rate itself is indifferent when consistent or lumped mass are used.

The energy budget are shown in Figures 8 and 9 using consistent mass for Gα and GEMM+ξ, respectively. No excessive numerical dissipation is observed. Indeed, as in the previous example, the numerical dissipation is almost zero.

Table VI. Maximum level of the dissipation at the end of each analysis and time-to-failure (Section 3.3).

ρ_∞	C^0	C^1	C^2	C^3	C^4
	Gα with consistent mass				
0.50	$1 \cdot 10^{-1}\%$	$1 \cdot 10^{-1}\%$	$1 \cdot 10^{-1}\%$	$1 \cdot 10^{-1}\%$	$1 \cdot 10^{-1}\%$
0.95	$2 \cdot 10^{-4}\%$	$2 \cdot 10^{-4}\%$	$2 \cdot 10^{-4}\%$	$1 \cdot 10^{-4}\%$	$1 \cdot 10^{-4}\%$
0.99	$1 \cdot 10^{-2}\%$ (0.86)	$3 \cdot 10^{-3}\%$	$5 \cdot 10^{-5}\%$	$1 \cdot 10^{-4}\%$ (0.92)	$3 \cdot 10^{-3}\%$ (0.89)
1.00	$7 \cdot 10^{-7}\%$ (0.53)	0% (0.61)	0% (0.52)	0% (0.54)	0% (0.53)
	Gα with lumped mass				
1.00	0.49%	0.45%	0.41%	0.30%	0.41%
	GEMM+ξ with consistent mass				
1.00	$\uparrow 2 \cdot 10^{-4}\%$	$\uparrow 2 \cdot 10^{-4}\%$	$\uparrow 2 \cdot 10^{-4}\%$	$\uparrow 2 \cdot 10^{-2}\%$	$\uparrow 4 \cdot 10^{-2}\%$
	GEMM+ξ with lumped mass				
1.00	0.46%	0.45%	0.42%	0.37%	0.17%
	$\uparrow$ implies in the growing of the total energy.				
	$(t_f \cdot 10^1) \rightarrow$ time-to-failure in seconds.				

Gα, generalized-α; GEMM+ξ, generalized energy–momentum method + ξ.
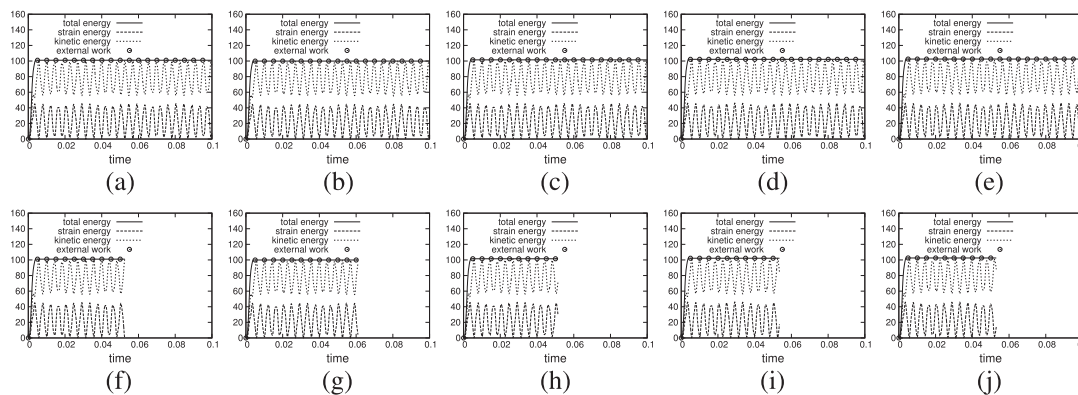
Figure 8. Energy of toss rule and generalized α with consistent mass. (a) $\rho_\infty = 0.95, C^0$; (b) $\rho_\infty = 0.95, C^1$; (c) $\rho_\infty = 0.95, C^2$; (d) $\rho_\infty = 0.95, C^3$; (e) $\rho_\infty = 0.95, C^4$; (f) $\rho_\infty = 1.00, C^0$; (g) $\rho_\infty = 1.00, C^1$; (h) $\rho_\infty = 1.00, C^2$; (i) $\rho_\infty = 1.00, C^3$; and (j) $\rho_\infty = 1.00, C^4$.

3.4. Toss rule – space movement

This problem was studied in [17], where different time integration schemes are employed in order to show the intrinsic conservative properties of GEMM+ξ. A numerical investigation of the spatial movement of a toss rule is performed in this example, where a geometrically nonlinear dynamic analysis is carried out.

In this example, the previous application is modified in order to demonstrate the computational performance of the proposed numerical model under three-dimensional motions. Geometry and load time history presented in Figure 10(a) and (b) are the same as those presented in the previous example (Section 3.3). It is important to notice that loads are applied in order to produce the spatial motion of the rule, which is free to fly. Computational parameters adopted here are shown in Table VII. It is worth noting that only consistent mass is employed in the remaining examples. Number and distribution (L, h, w) of elements over the physical space referring to the rule are again given according to
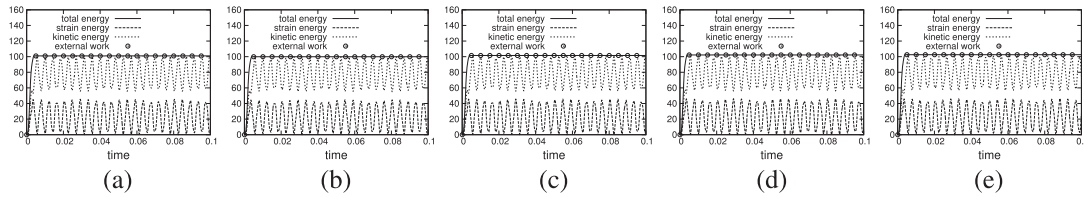
Figure 9. Energy of toss rule and generalized energy–momentum method + ξ with consistent mass. (a) $\rho_\infty = 1.00, C^0$; (b) $\rho_\infty = 1.00, C^1$; (c) $\rho_\infty = 1.00, C^2$; (d) $\rho_\infty = 1.00, C^3$; and (e) $\rho_\infty = 1.00, C^4$.

Table VII. Computational parameters employed in the toss rule analysis.

Control mesh	Number of elements	Continuity class	Spectral radius – ρ_∞	Degrees (p, q, r)
Gα with consistent mass				
$66 \times 3 \times 6$	$13 \times 1 \times 1$	C^0	0.90; 1.00	5, 2, 5
$66 \times 3 \times 6$	$16 \times 1 \times 1$	C^1	0.90; 1.00	5, 2, 5
$66 \times 3 \times 6$	$21 \times 1 \times 1$	C^2	0.90; 1.00	5, 2, 5
$66 \times 3 \times 6$	$31 \times 1 \times 1$	C^3	0.90; 1.00	5, 2, 5
$66 \times 3 \times 6$	$61 \times 1 \times 1$	C^4	0.90; 1.00	5, 2, 5
GEMM+ξ with consistent mass				
$66 \times 3 \times 6$	$13 \times 1 \times 1$	C^0	0.99, 0,999, 1.00	5, 2, 5
$66 \times 3 \times 6$	$16 \times 1 \times 1$	C^1	0.99, 0,999, 1.00	5, 2, 5
$66 \times 3 \times 6$	$21 \times 1 \times 1$	C^2	0.99, 0,999, 1.00	5, 2, 5
$66 \times 3 \times 6$	$31 \times 1 \times 1$	C^3	0.99, 0,999, 1.00	5, 2, 5
$66 \times 3 \times 6$	$61 \times 1 \times 1$	C^4	0.99, 0,999, 1.00	5, 2, 5

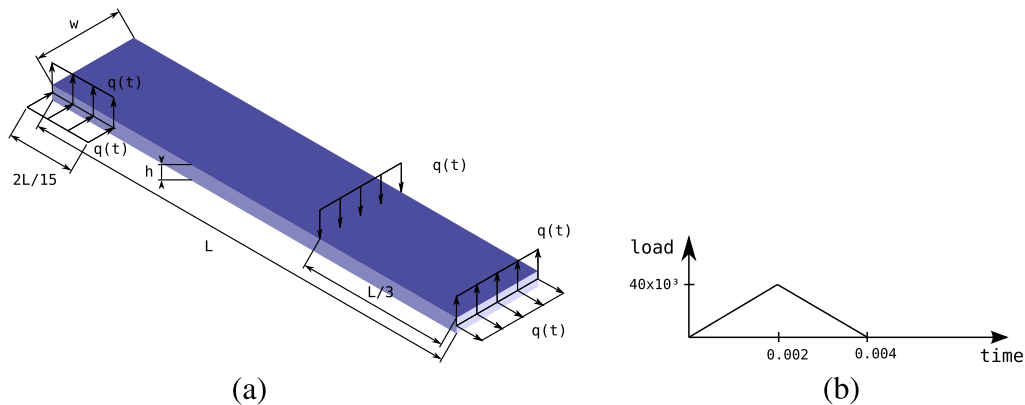Gα, generalized-α; GEMM+ξ, generalized energy–momentum method + ξ.

Figure 10. Geometry and boundary conditions of the toss rule: $L = 0.3$ m; $h = 0.002$ m; and $w = 0.06$ m. (a) Geometry and boundary conditions; and (b) load $q(t)$.

the continuity class, where the element configurations (13×1×1), (16×1×1), (21×1×1), (31×1×1), and (61 × 1 × 1) correspond to the continuity classes C^0, C^1, C^2, C^3, and C^4, respectively. In each simulation, the same number of degrees of freedom is used.

The dynamic responses obtained from the numerical analyses performed here are shown in Figure 11 for Gα with consistent mass, $\rho_\infty = 0.90$, and C^4. Linear and angular momentum are presented in Figure 11(a) and (b), respectively, while successive configurations are shown in Figure 11(c) in the interval [0.0 s, 0.04 s] with $\Delta t = 0.004$ s.

In Table VIII, the numerical dissipation at the end of each analysis and the time-to-failure are presented. Also, in Figure 12, the time evolution of the numerical dissipation is shown. From this
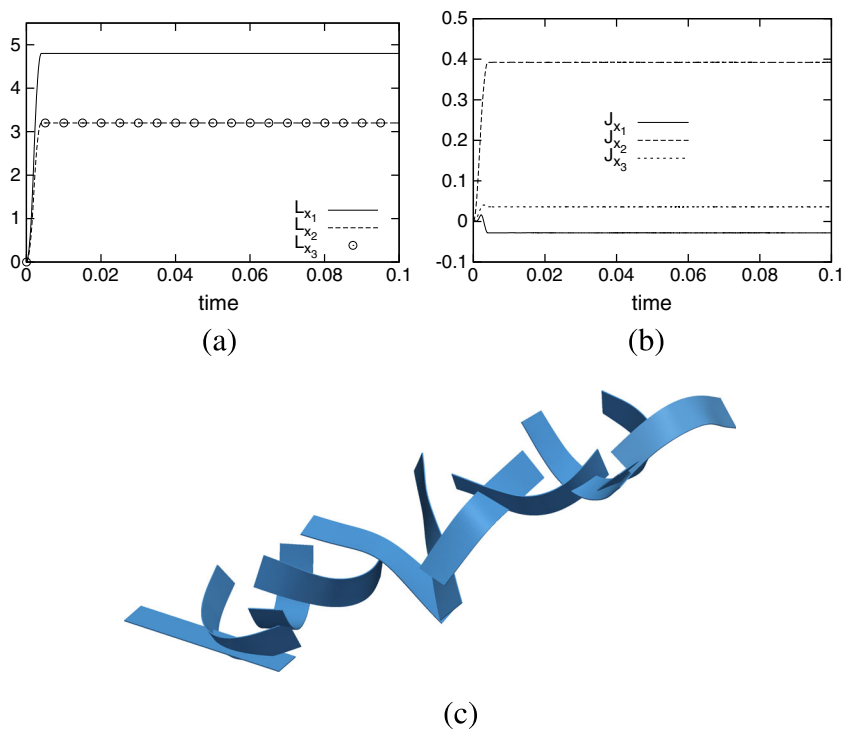
Figure 11. Successive configurations: generalized α. (a) Linear momentum, $\underline{L}$; (b) angular momentum, $\underline{J}$; and (c) $\rho_\infty = 0.90$ e C^4.

Table VIII. Maximum level of the dissipation at the end of each analysis and time-to-failure (Section 3.3).

ρ_∞	C^0	C^1	C^2	C^3	C^4
			$G\alpha$ with consistent mass		
0.90	6.3%	7.5%	6.8%	6.8%	6.0%
1.00	0% (3.2)	0% (3.5)	0% (3.1)	0% (3.0)	0% (3.3)
			GEMM+ξ with consistent mass		
0.99	6.9%	6.3%	6.3%	6.4%	5.3%
0.999	↑ 10.1% (4.8)	↑ 8.3% (4.5)	↑ 22.8% (8.6)	↑ 17.6% (5.8)	↑ 15.4% (8.7)
1.00	↑ 7.6% (4.4)	↑ 10.2% (4.5)	↑ 13.1% (4.8)	↑ 14.9% (4.8)	↑ 26.2% (8.1)
			↑ implies in the growing of the total energy.		
			$(t_f \cdot 10^2) \rightarrow$ time-to-failure in seconds.		

$G\alpha$, generalized-α; GEMM+ξ, generalized energy–momentum method + ξ.

figure, one can always observe that a higher continuity exhibits a less amount of numerical dissipation. The convergence rates are about 1.8 and 2.0 for force and displacement, respectively, in $G\alpha$ method, while in GEMM+ξ, a convergence rate about 1.6 and 1.8 for force and displacement are observed, respectively.

In Figures 13 and 14, results in terms of energy are presented, for both $G\alpha$ and GEMM+ξ, respectively. Results shown here demonstrate again a sudden interruption of the time integration process when a spectral radius equal to $\rho_\infty = 1.00$ is considered (no numerical dissipation), independently of the continuity class used, for $G\alpha$ method with consistent mass. On the other hand, when GEMM+ξ is employed with spectral radii equal to $\rho_\infty = 1.00$ and $\rho_\infty = 0.999$, the total energy is continuously increased until the failure in the time integration occurs. Stable solutions with decay
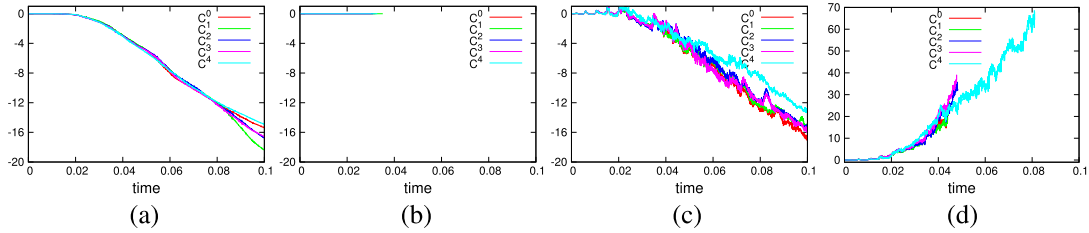
Figure 12. Numerical dissipation. (a) Generalized $\alpha, \rho_\infty = 0.90$; (b) generalized $\alpha, \rho_\infty = 1.00$; (c) generalized energy–momentum method $+ \xi, \rho_\infty = 0.99$; and (d) generalized energy–momentum method $+ \xi, \rho_\infty = 1.00$.
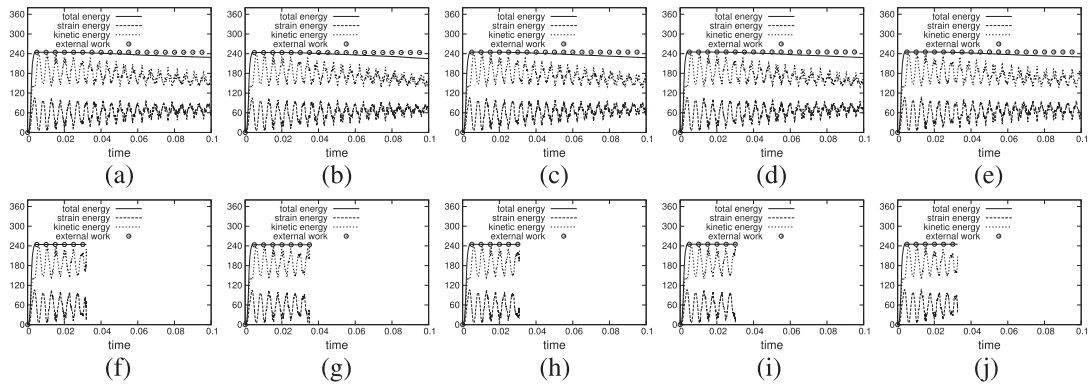

Figure 13. Energy of toss rule and generalized α with consistent mass. (a) $\rho_\infty = 0.90, C^0$; (b) $\rho_\infty = 0.90, C^1$; (c) $\rho_\infty = 0.90, C^2$; (d) $\rho_\infty = 0.90, C^3$; (e) $\rho_\infty = 0.90, C^4$; (f) $\rho_\infty = 1.00, C^0$; (g) $\rho_\infty = 1.00, C^1$; (h) $\rho_\infty = 1.00, C^2$; (i) $\rho_\infty = 1.00, C^3$; and (j) $\rho_\infty = 1.00, C^4$.
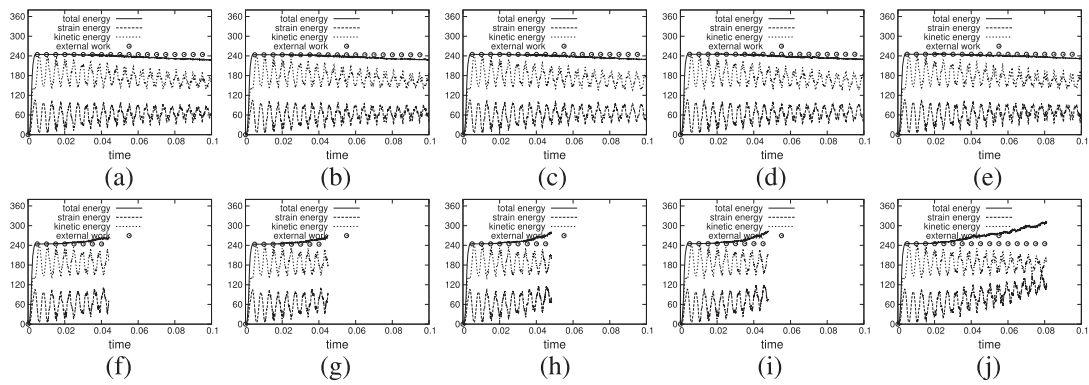

Figure 14. Energy of toss rule and generalized energy–momentum method $+ \xi$ with consistent mass. (a) $\rho_\infty = 0.99, C^0$; (b) $\rho_\infty = 0.99, C^1$; (c) $\rho_\infty = 0.99, C^2$; (d) $\rho_\infty = 0.99, C^3$; (e) $\rho_\infty = 0.99, C^4$; (f) $\rho_\infty = 1.00, C^0$; (g) $\rho_\infty = 1.00, C^1$; (h) $\rho_\infty = 1.00, C^2$; (i) $\rho_\infty = 1.00, C^3$; and (j) $\rho_\infty = 1.00, C^4$.

of the total energy are obtained with spectral radii $\rho_\infty = 0.90$ and $\rho_\infty = 0.99$ with Gα method and GEMM+ξ, respectively.

3.5. 'Snap-through' of a cylindrical shell

The snap-through phenomenon occurring in a hinge-supported cylindrical shell subject to a concentrated load is investigated here. Geometry and boundary conditions are shown in Figure 15(a), while load description for the present simulation is shown in Figure 15(b). Material properties of the
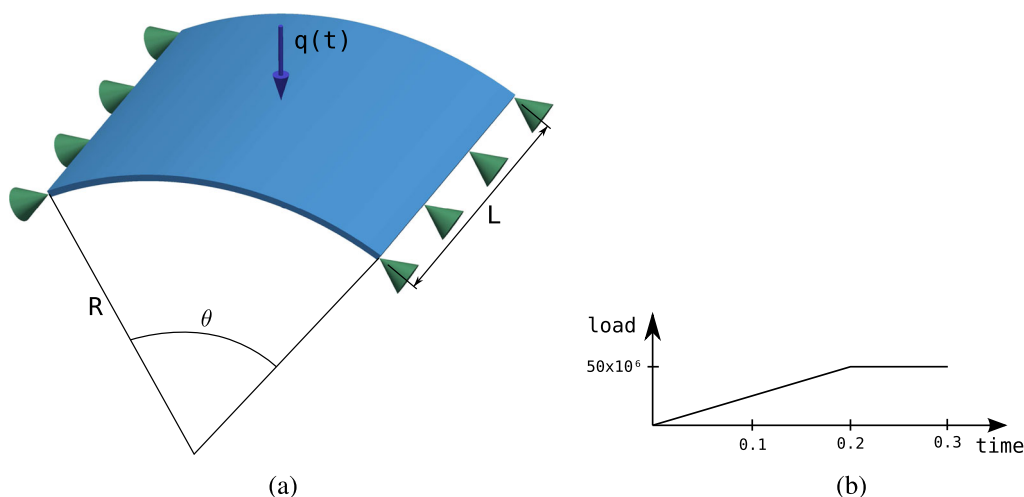
Figure 15. Geometry and boundary conditions of cylindrical shell: $R = 5.0$ m; $L = 5.0$ m; and $\theta = 60°$.
(a) Geometry and boundary conditions; and (b) load.

Table IX. Geometrical and load characteristics for
the cylindrical shell analysis.

Young modulus	E (N/m^2)	$2.0 \cdot 10^{11}$
Poisson coefficient	ν	0.25
Specific mass	ρ (kg/m^3)	$1.0 \cdot 10^4$
Damping coefficient	ϕ	0.0
Time step	Δt (s)	$5.0 \cdot 10^{-4}$

Table X. Computational parameters employed in the cylindrical shell analysis.

Control mesh	Number of elements	Continuity class	Spectral radius – ρ_∞	Degrees (p, q, r)
		Gα with consistent mass		
$18 \times 18 \times 5$	$8 \times 8 \times 2$	C^1	0.50; 0.90; 0.95	5, 5, 2
$13 \times 13 \times 5$	$4 \times 4 \times 2$	C^4	0.50; 0.90; 0.95	5, 5, 2
		GEMM+ξ with consistent mass		
$18 \times 18 \times 5$	$8 \times 8 \times 2$	C^1	0.90; 0.95	5, 5, 2
$13 \times 13 \times 5$	$4 \times 4 \times 2$	C^4	0.90; 0.95	5, 5, 2

For all simulations C^0 through the thickness is used,
while the continuity class over the surface is indicated in this table.

Gα, generalized-α; GEMM+ξ, generalized energy–momentum method + ξ.

structure as well as the time step adopted in the time integration procedure are found in Table IX. Information on computational parameters used in the parametric studies carried out here are summarized in Table X. Number and distribution (L, w, h) of elements over the physical space referring to the cylindrical shell are given as follows: the continuity class C^1 corresponds to the continuity class employed over the shell surface, where the element configuration (8×8) is adopted. The computational mesh related to the continuity class C^4 presents (4×4) elements over the shell surface. Along the shell thickness, two elements of C^0 continuity are used in both meshes, such that the control points associated with the middle surface of the cylindrical shell become interpolatory and the boundary conditions corresponding to hinge supports can be appropriately imposed.
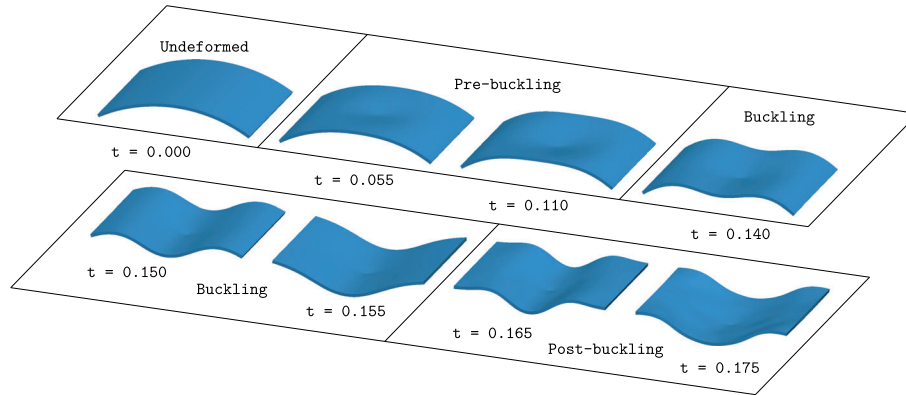
Figure 16. Successive configurations: generalized energy–momentum method + ξ with $\rho_\infty = 0.90$ and C^4.

Table XI. Maximum level of the dissipation at the end of each analysis and time-to-failure.

ρ_∞	C^1	C^4
	Gα with consistent mass	
0.50	49.2%	49.3%
0.90	5.4%	5.0%
0.95	0.8% (0.27)	0.5% (0.27)
	GEMM+ξ with consistent mass	
0.90	54.7%	56.3%
0.95	42.0%	48.2%
	$\uparrow$ implies in the growing of the total energy.	
	$(t_f) \rightarrow$ time-to-failure in seconds.	

Gα, generalized-α; GEMM+ξ, generalized energy–momentum method + ξ.

In Figure 16, successive configurations for simulation carried out with GEMM+ξ are presented. In this sequence, at early stages of analysis the pre-buckling stage is defined and only lower frequencies are excited. When stiffness matrix is singular, around $t = 0.155$, the buckling is identified. After that, the membrane stiffness is recovered, giving rise to a high-frequency vibration in the post-buckling stage. In Table XI, the numerical dissipation at the end of each analysis and the time-to-failure are presented.

When the total number of degrees of freedom is maintained constant, as in the previous examples, a higher continuity exhibits less amount of numerical dissipation. However, one can expect that by using higher resolutions (concerning the total number of degrees of freedom), less numerical dissipation is obtained. Indeed, in this example, when the continuity class is reduced from C^4 to C^1, the number of elements is duplicated. Nevertheless, most of simulations carried out in this example show more numerical dissipation when a lower continuity is adopted. As a matter of fact, only when GEMM+ξ with $\rho_\infty = 0.95$ is employed can this statement not be verified.

From Figure 17, it may be stated that in general C^4 continuity shows less numerical dissipation than C^1 continuity. Naturally, the effects induced by the spectral radius are clearly noted, because the numerical dissipation is increased when the spectral radius is decreased. A stable solution is obtained for $\rho_\infty = 0.50$ for Gα method. For GEMM+ξ, a stable solution is obtained for $\rho_\infty = 0.95$. Considering that the time step is refined enough at an early stage (pre-buckling stage) of the simulation where vibration is dominated by lower modes, numerical dissipation is not observed. After that, the time step becomes marginal once the high frequencies are excited, i.e., the time step seems to be too large to correctly solve the higher modes; therefore, one can observe numerical
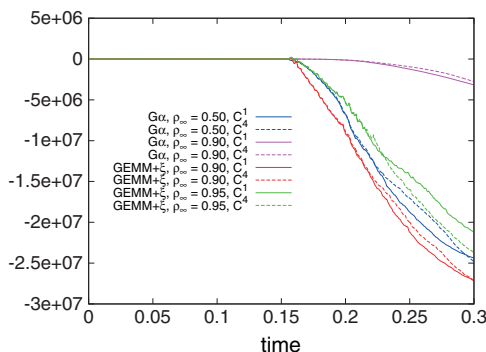
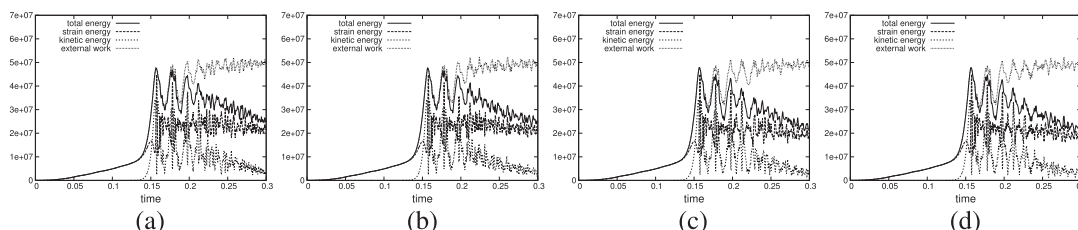Figure 17. Numerical dissipation. GEMM+ξ, generalized energy–momentum method + ξ.

Figure 18. Energy of cylindrical shell, and generalized α (Gα) and generalized energy–momentum method + ξ (GEMM+ξ) with consistent mass. (a) $\rho_\infty = 0.50, C^1$, Gα; (b) $\rho_\infty = 0.50, C^4$, Gα; (c) $\rho_\infty = 0.90, C^1$, GEMM+ξ; and (d) $\rho_\infty = 0.90, C^4$, GEMM+ξ.
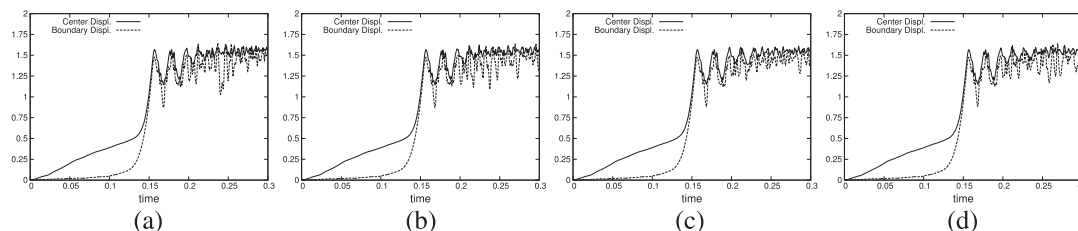

Figure 19. Displacement at point load location of cylindrical shell, and generalized α (Gα) and generalized energy–momentum method + ξ (GEMM+ξ) with consistent mass. (a) $\rho_\infty = 0.50, C^1$, Gα; (b) $\rho_\infty = 0.50, C^4$, Gα; and (c) $\rho_\infty = 0.90, C^1$, GEMM+ξ; and (d) $\rho_\infty = 0.90, C^4$, GEMM+ξ.

dissipation, only in buckling and post-buckling stages. Nevertheless, the amount of numerical damping must be carefully controlled in order to obtain accurate results. It is observed that the convergence rates of this analysis are about 1.5 and 2.0 for force and displacement, respectively, in Gα method, while in GEMM+ξ, convergence rates about 1.7 and 2.0 for force and displacement, respectively, are observed.

Figure 18(a) and (b) and Figure 18(c) and (d) present results in term of energy, for Gα method and GEMM+ξ with consistent mass, respectively, while Figure 19(a) and (b) and Figure 19(c) and (d) present the dynamic responses that are given in terms of vertical displacements measured at the position where the load is applied, for Gα method and GEMM+ξ with consistent mass, respectively. In addition, the displacement response is also evaluated at the middle point on the free edge of the cylindrical shell.

In Figure 20(a), results obtained in this work are compared with numerical predictions obtained in [17] and using the commercial package ABAQUS (ABAQUS Inc., Palo Alto, CA, USA) (with an explicit solver), while in Figure 20(b), it is compared with those obtained in [37] and [9]. In Figure 20(c), a comparison between Gα method and GEMM+ξ is presented. The present results
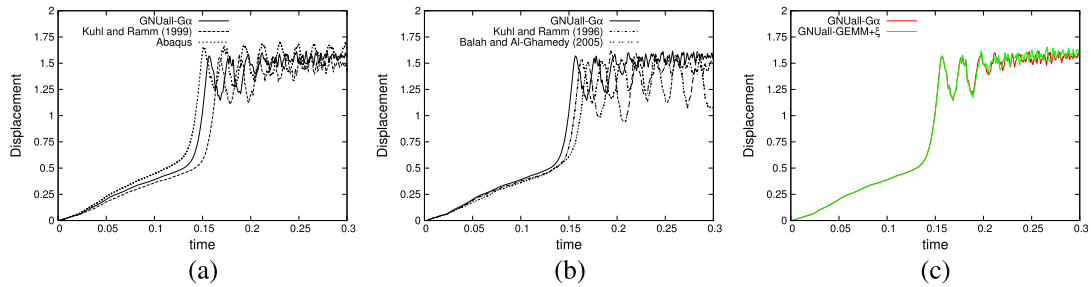
Figure 20. Comparisons of vertical displacement of the middle point. (a) Generalized α (Gα) ($\rho_\infty = 0.50, C^4$) versus [17]; (b) Gα ($\rho_\infty = 0.50, C^4$) versus [9, 37]; and (c) Gα ($\rho_\infty = 0.50, C^4$) versus generalized energy–momentum method + ξ (GEMM+ξ) ($\rho_\infty = 0.95, C^4$).

correspond to the numerical analysis performed considering the following spectral radius and continuity class: $\rho_\infty = 0.50, C^4$ and $\rho_\infty = 0.95, C^4$ for Gα method and GEMM+ξ, respectively. An overall good agreement can be observed, except for the solution presented in [9], where the higher modes are not present and the energy is concentrated on the lower modes.

3.6. Discussion of results

Several numerical examples are described in the previous sections. Simulations dealing with geometrically nonlinear behavior in elastodynamic field are investigated with respect to numerical instability and energy–momentum conservation. Both features, numerical stability and energy–momentum conservation, are parametrically studied with respect to spectral radius and continuity class as well as with respect to lumped and consistent mass matrices. Furthermore, two time integrators, Gα and GEMM+ξ, based on equilibrium at intermediate level of the time increment were implemented.

Concerning the energy–momentum conservation, in general it is possible to observe that both, Gα method and GEMM+ξ, show less numerical dissipation when a high continuity class is adopted. This statement is based on the examples in Sections 3.4 and 3.5 (see, for instance, Figures 12 and 17, which present the time evolution of the dissipation) where the numerical dissipation are more significant. On the other hand, for Gα and GEMM+ξ, the energy and momentum are perfectly conserved for the examples presented in Sections 3.2 and 3.3, even when a lumped mass is employed.

A time step size that is several orders of magnitude less than the oscillation period may be considered a refined time step. From the linear dynamic theory, one can define that a time-step size is refined enough if, at least, it is lower than one order of magnitude of the oscillation period. Therefore, in the nonlinear case, in the presence of higher frequencies, if a small time step is not adopted, an insufficient amount of dissipation may lead to numerical instability, as observed in the examples Sections 3.4 and 3.5. Also, numerical dissipation is strongly related to the time-step size if a spectral radius less than the unity is adopted, i.e., for a certain spectral radius, by increasing the time-step size, the numerical dissipation is also increased. Therefore, the numerical dissipation acts as a damper of spurious modes and/or ill-resolved scales.

It is worth noting that in the last example (Section 3.5) until $t \approx 0.15$ s when lower modes are excited (and the time-step size is refined enough when compared with the oscillation period), there is no dissipation and it is possible to solve well all scales, as expected. After this time, higher frequencies are excited and the time-step size becomes too large when compared with oscillation period. Therefore, spurious and ill-resolved scales are correctly dissipated. The dissipation grows, approximately with a constant slope.

Regarding the numerical stability, it is evident that GEMM+ξ is most robust than Gα, because of an additional dissipation parameter that leads to more stable algorithms. Also, when GEMM+ξ with consistent mass is employed, it is observed that a higher continuity can postpone the numerical instability, as shown in the examples Sections 3.2 and 3.4. Unfortunately, this behavior cannot be observed neither when Gα is employed nor when lumped mass description is used.

Another important issue is related to numerical model adopted in this work, where a NURBS solid model was employed. This fact means that in solid models there are more vibration modes involved and indeed they are more complex than those obtained with beam or shell models. Thus, stable analysis with conservative properties may be more difficult to obtain with a complete model obtained from a general theory of continuum mechanics.

In particular, some aspects may be pointed out.

- In the first example Section 3.2, there is a dependence between the numerical stability and the continuity class when GEMM+ξ with consistent mass is employed, there is an evident and monotonic dependence, and by increasing the continuity class, the numerical instability is postponed. Actually, only for continuity C^4 is the final convergence achieved.
- In the second example Section 3.3, the range of stable spectral radius obtained with the IsoGeometric model is slightly wider than that presented by the finite element model proposed in [14]. Indeed, a stable analysis with conservation of the energy and momentum was possible with spectral radii from 0.5 to 0.95 using Gα and also with a spectral radius equal to one when GEMM+ξ is employed. When Gα with consistent mass is used, there is not a dependence between the numerical stability and the continuity class. For lumped mass, high continuity seems to have a detrimental effect on the numerical stability. For simulations carried out with GEMM+ξ, numerical instability did not occur. Also, the total energy and momentum are perfectly conserved.
- In the third example Section 3.4, a marginal time step led to an unstable analysis when a spectral radius equal to one was used and a stable analysis was only possible with spectral radii $\rho_\infty = 0.90$ for Gα and $\rho_\infty = 0.99$ for GEMM+ξ. When Gα method with $\rho_\infty = 1.00$ was employed, the numerical instability occurred at $t \approx 0.3$ independently of the continuity, however, without energy losses. On the other hand, when GEMM+ξ with $\rho_\infty = 1.00$ was employed, the higher continuity postponed the numerical instability. However, the energy increased, giving rise to the numerical instability. Nevertheless, higher continuity produced less numerical dissipation or a lower growth of the total energy.
- In the fourth example Section 3.5, a stable analysis was only possible with spectral radii $\rho_\infty = 0.90$ for Gα and $\rho_\infty = 0.95$ for GEMM+ξ, although the total dissipation in any stable analysis has the same order of magnitude. Also, as in the previous example, simulations carried out with high continuity exhibited in general less numerical dissipation.

4. CONCLUSIONS

The application of the Gα method and GEMM+ξ to nonlinear dynamics using a NURBS-based element with a corotational approach was presented. Several numerical examples exhibiting highly nonlinear dynamic behavior were carried out. Improvements provided by the NURBS basis functions produced great impact over the conservation of the energy–momentum and numerical stability in the nonlinear dynamic field. Particularly, it was shown that high continuity can postpone the numerical instability when GEMM+ξ with consistent mass is employed. In addition, it was demonstrated that by increasing the continuity class, the numerical dissipation is decreased (if the spectral radius is less than the unity). Regarding the numerical predictions obtained with Gα and GEMM+ξ, results were approximately the same in most of the cases analyzed here, where the accuracy level of the present model was also demonstrated taking into account the excellent agreement with reference results.

REFERENCES

1. Newmark N. A method of computation for structural dynamics. *Journal of Engineering Mechanics ASCE* 1959; **85-EM3**:67–94.
2. Goudreau G, Taylor R. Evaluation of numerical methods in elastodynamics. *Computer Methods in Applied Mechanics and Engineering* 1973; **2**:69–97.
3. Hilber H, Hughes T, Taylor R. Improved numerical dissipation for the time integration algorithms in structural dynamics. *Earthquake Engineering and Structural Dynamics* 1977; **5**:283–292.
4. Wood W, Bossak M, Zienkiewicz O. An alpha modification of Newmark's method. *International Journal for Numerical Methods in Engineering* 1980; **15**:1562–1566.
5. Chung J, Hulbert G. A time integration algorithm for structural dynamics with improved numerical dissipation: the generalized-α method. *Journal of Applied Mechanics, Transactions of the ASME* 1993; **60**:371–375.
6. Belytschko T, Schoeberle D. On the unconditional stability of an implicit algorithm for nonlinear structural dynamics. *ASME Journal of Applied Mechanics* 1975; **17**:865–869.
7. Hughes T, Caughey T, Liu W. Finite element methods for nonlinear elastodynamics which conserve energy. *Journal of Applied Mechanics* 1978; **45**:366–370.
8. Ortiz M. A note on energy conservation and stability of nonlinear time-stepping algorithms. *Computer and Structures* 1986; **24**:167–168.
9. Kuhl D, Ramm E. Constraint energy momentum algorithm and its application to nonlinear dynamics of shells. *Computer Methods in Applied Mechanics and Engineering* 1996; **136**:293–315.
10. Simo J, Tarnow N. The discrete energy-momentum method, conserving algorithms for nonlinear elastodynamics. *Journal of Applied Mathematics and Physics* 1992; **43**:757–792.
11. Gonzalez G. Exact energy and momentum conserving algorithms for general models in nonlinear elasticity. *Computer Methods in Applied Mechanics and Engineering* 2000; **190**:1763–1783.
12. Laursen T, Meng X. A new solution procedure for application of energy-conserving algorithms to general constitutive models in nonlinear elastodynamics. *Computer Methods in Applied Mechanics and Engineering* 2001; **190**:6309–6322.
13. Noels L, Stainier L, Ponthot J. An energy-momentum conserving algorithm for non-linear hypoelastic constitutive models. *International Journal for Numerical Methods in Engineering* 2004; **59**:83–114.
14. Braun A, Awruch A. Geometrically non-linear analysis in elastodynamics using the eight-node finite element with one-point quadrature and the generalized-α method. *Latin American Journal of Solids and Structures* 2008; **5**:17–45.
15. Romero I. An analysis of the stress formula for energy-momentum methods in nonlinear elastodynamics. *Computational Mechanics* 2012; **50**:603–610.
16. Kuhl D, Crisfield M. Energy-conserving and decaying algorithms in non-linear structural dynamics. *International Journal for Numerical Methods in Engineering* 1999; **45**:569–599.
17. Kuhl D, Ramm E. Generalized energy-momentum method for non-linear adaptive shell dynamics. *Computer Methods in Applied Mechanics and Engineering* 1999; **178**:343–366.
18. Armero F, Petocz E. Formulation and analysis of conserving algorithms for frictionless dynamic contact-impact problems. *Computer Methods in Applied Mechanics and Engineering* 1998; **158**:269–300.
19. Crisfield M, Galvanetto U, Jelenic G. Dynamics of 3-D co-rotational beams. *Computational Mechanics* 1997; **20**:507–519.
20. Armero F, Romero I. On the formulation of high-frequency dissipative time-stepping algorithms for nonlinear dynamics. Part II: high order methods. *Computer Methods in Applied Mechanics and Engineering* 2001; **190**:6783–6824.
21. Armero F, Romero I. On the formulation of high-frequency dissipative time-stepping algorithms for nonlinear dynamics. Part i: low order methods for two model problems and nonlinear elastodynamics. *Computer Methods in Applied Mechanics and Engineering* 2001; **190**:2603–2649.
22. Erlicher S, Bonaventura L, Bursi O. The analysis of the generalized-α method for non-linear dynamic problems. *Computational Mechanics* 2002; **28**:83–104.
23. Espath L, Braun A, Awruch A, Maghous S. NURBS-based three-dimensional analysis of geometrically nonlinear elastic structures. *European Journal of Mechanics A/Solids* 2014; **43**:373–390.
24. Malvern L. *Introduction to the Mechanics of a Continuous Medium*. Prentice Hall: Englewood Cliffs, New Jersey, 1969.
25. Hughes T, Winget J. Finite rotations effects in numerical integration of rate constructive equations arising in large deformation analysis. *International Journal for Numerical Methods in Engineering* 1980; **15**:1862–1867.
26. Bazilevs Y, Calo V, Cottrell J, Hughes T, Reali A, Scovazzi G. Variational multiscale residual-based turbulence modeling for large eddy simulation of incompressible flows. *Computer Methods in Applied Mechanics and Engineering* 2007; **197**:173–201.
27. Benson D, Bazilevs Y, Hsu M, Hughes T. Isogeometric shell analysis: the Reissner-Mindlin shell. *Computer Methods in Applied Mechanics and Engineering* 2010; **199**:276–289.
28. Espath L, Linn R, Awruch A. Shape optimization of shell structures based on NURBS description using automatic differentiation. *International Journal for Numerical Methods in Engineering* 2011; **88**(7):613–636.
29. Wen WB, Jian KL, Luo SM. An explicit time integration method for structural dynamics using septuple B-spline functions. *International Journal for Numerical Methods in Engineering* 2014; **97**(9):629–657.

30. Linn R, Espath L, Awruch A. Optimal shape of axisymmetric solids using NURBS and automatic differentiation. *Applied Mathematical Modelling* 2014; **38**(4):1385–1402.

31. Cottrell J, Hughes T, Bazilevs Y. *Isogeometric Analysis: Towards Integration of CAD and FEA*. Wiley: The Atrium, Suthern Gate, Chichester, West Sussex, 2009.

32. Piegl LA, Tiller W. *The NURBS Book* (2nd edn). Springer: Berlin Heidelberg, 1997.

33. Cox M. The numerical evaluation of B-spline. *Institute of Mathematics and Its Applications* 1972; **10**(1):134–149.

34. deBoor C. On calculating with B-spline. *Approximation Theory* 1972; **6**(1):50–72.

35. Bathe KJ. *Finite Element Procedures* (2nd edn). Prentice Hall: Upper Saddle River, New Jersey, 1996.

36. Bathe KJ, Baig MMI. On a composite implicit time integration procedure for nonlinear dynamics. *Computers and Structures* 2005; **83**:2513–2524.

37. Balah M, Al-Ghamedy HN. Energy-momentum conserving algorithm for nonlinear dynamics of laminated shells based on a third-order shear deformation theory. *Journal of Engineering Mechanics ASCE* 2005; **131**:12–22.